ACS OMEGA

Open Access

This article is licensed under CC-BY-NC-ND 4.0

http://pubs.acs.org/journal/acsodf

Article

Potent and Versatile Biogenically Synthesized Alumina/Nickel Oxide Nanocomposite Adsorbent for Defluoridation of Drinking Water

Seham S. Alterary*

Cite This: *ACS Omega* 2024, 9, 23220−23240

Read Online

ACCESS | Metrics & More | Article Recommendations

ABSTRACT: In the present work, an extract of *Salvia officinalis* leaves was used to synthesize an alumina/NiO nanocomposite by the coprecipitation method. First, the shape and surface content of the synthesized adsorbent were determined. Scanning electron microscopy images showed the production of nanospheres and nanorods with sizes between 35 and 50 nm. X-ray diffraction measurement revealed strong, high-intensity peaks, confirming the preparation of a highly crystalline alumina/nickel oxide nanocomposite. Then, the pure nanoalumina, nickel oxide, and functionalized alumina/nickel oxide nanocomposite for water defluoridation were investigated under various conditions, for example, stirring period, pH, and initial fluoride concentration. Defluoridation with greener alumina, nickel oxide, and alumina/nickel oxide nanocomposite lasted 120 min at adsorbent dosages of 0.8 g/L in a pH 7 solution. The adoption process for the three sorbents matches the Langmuir adsorption isotherm. The process dynamics were explored using pseudo-second-order and first-order kinetics. The water quality after treatment met drinking water requirements, proving the viability of using nanoparticles for drinking water defluoridation. This work confirmed effective water defluoridation in the crystalline phase using synthesized nanoalumina, nickel oxide, and their nanocomposite, which highlights their importance for future drinking water defluoridation.

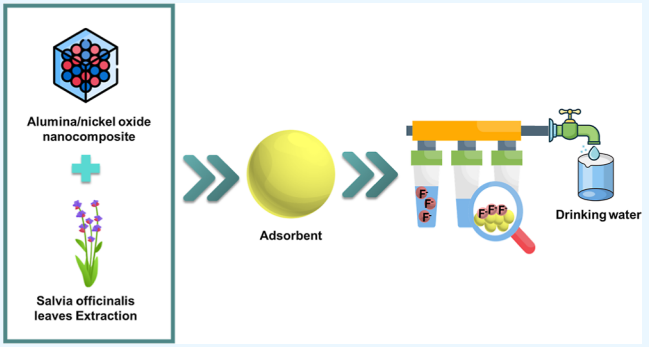

1. INTRODUCTION

Water contamination is one of the world's main issues today. Because of their toxicity, accumulation in the food chain, and presence in nature, heavy metals in water pose a serious hazard to both people and animals.[1] There is a severe drinking water scarcity, with about 42% of the global population without access to clean and safe drinking water.[2] In many developing nations, groundwater is used for residential purposes, mostly in rural areas. However, depending on the geographical location, groundwater contains significant concentrations of minerals such as fluoride ions, making it dangerous to drink.[3,4] Fluoride is an anionic main pollutant in many developing nations. It causes fluorosis of bone, dental fluorosis, Alzheimer's disease, and cancer in many impoverished individuals who are unable to treat their drinking water to suggested allowable limits.[5,6] The WHO has defined the permissible fluoride concentration in drinking water as 1.5 mg/L,[7] and drinking water above this limit for an extended period of time can lead to fluorosis, a condition that primarily affects bones and teeth and, in severe cases, results in neuro-degenerative diseases.[8]

Water defluoridation procedures such as ion exchange, adsorption, nanofiltration, electrocoagulation, and membrane separation have all been documented.[9] Adsorption is still a common approach for water defluoridation because it is a cost-effective way of producing high-quality treated effluent while also providing design and scale-up flexibility.[10,11] Metals and metal oxides, carbon-based, natural and synthetic polymers, and biomaterials have all been described as adsorbents for water defluoridation.[5,12,13]

Adsorbent-based alumina is commonly used for removal of fluoride from water because fluoride has high electronegativity and affinity to alumina. Alumina is also a cost-effective solution since it is abundant or quickly synthesized and may be employed in water treatment.[14] In nano dimensions, elemental structural quality would be improved.[15] The procedures employed to create nanoparticles (NPs) influence their chemical and physical characteristics.[16] Inorganic substances can be oxidized using NPs as a catalyst.[17,18] Ultrafine NiO particles of the same size are widely employed in a variety of sectors, including the fabrication of films, magnetic components, ceramics, and batteries.[19−21]

Nanosized metal oxides have drawn attention from researchers because of their various technological applications

Received: November 14, 2023
Revised: May 1, 2024
Accepted: May 9, 2024
Published: May 23, 2024

© 2024 The Author. Published by American Chemical Society

Scheme 1. Schematic Diagram for General Illustration of the Proposed Study

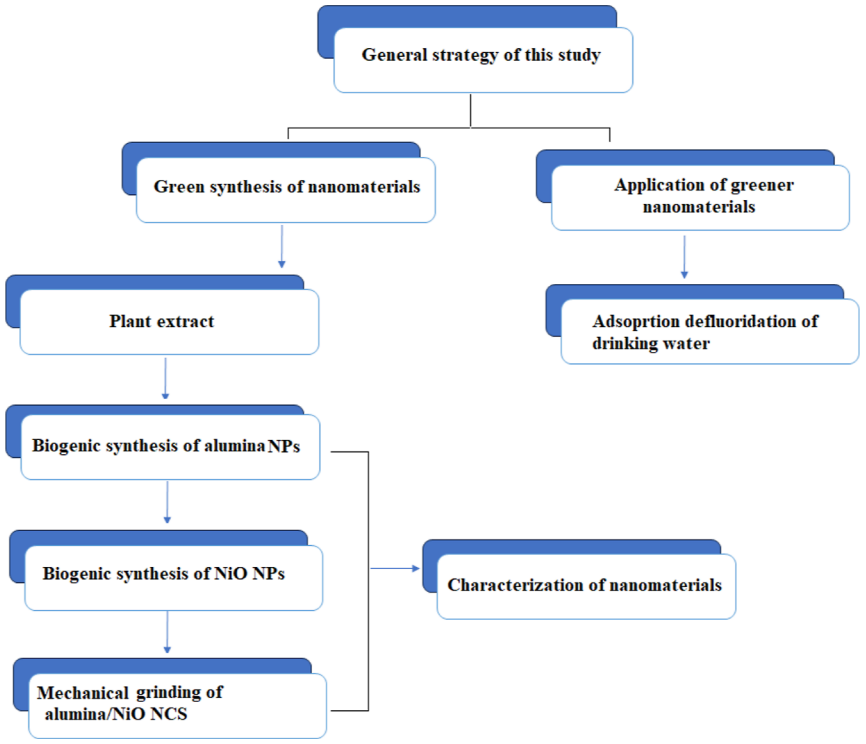

and properties. The chemical and physical characteristics of the synthesized NPs will depend on the particle shape.[22] With a wide band gap of 3.6−4.0 eV, NiO NPs are p-type semiconductors.[23] Since NiO NPs have a large surface area and can be used as catalysts and carriers, they are desirable absorbers.[24] It is possible to regulate the mobility of polluted ions in the environment using the NiO adsorbent. The adsorption capacity of nickel oxide NPs is appropriate for the removal of heavy metals, organic compounds, and anions from aqueous solutions due to their high surface area, low production cost, and inherent porosity.[25]

Furthermore, Al_2O_3 NPs and NiO NPs are among the most completely investigated metal oxides for water purification due to their mechanical robustness, high sorption capability, and wide surface area.[26−28] Green chemistry-based NP synthesis using plant extracts takes place at room temperature and pH, making it more cost-effective and environmentally friendly than damaging chemical or physical procedures.[29] Plant extracts are employed in biosynthesis, also known as green synthesis, to create metal oxide NPs from metal salts.[30]

The literature search revealed that several reports have described the green synthesis of alumina nanocomposites as potential sorbents for water treatment. These reports include green synthesis of iron−aluminum nanocomposites, aluminum alginate beads doped with metal oxides, a 3D hydrogel based on alumina and GO cellulose, and bionanocomposites based on fungal hyphae for fluoride removal from water.[31−34]

This work investigates the removal of fluoride from contaminated water using *Salvia officinalis* leaf extract and synthesized alumina NPs and NiO NPs. Sage (*S. officinalis* L) is a member of the mint family (Lamiaceae). Sage includes phenolics (rosmarinic, ferulic, caffeic, and vanillic acids), terpenoids, and flavonoids (quercetin, apigenin, and luteolin) among other bioactive components.[35] These phytocomponents function as reducing and stabilizing agents in the production of alumina NPs and NiO NPs, allowing for more control over the size and structure of the NPs. Metal organic chemical vapor deposition, polymer precursor method, high-energy milling, electrochemical treatment technique, and sol−gel technique are some of the methods used to synthesize Al_2O_3 NPs and NiO NPs.[36,37] The physical approach, as we all know, is both expensive and time-consuming. Numerous recent investigations have revealed that the coprecipitation method may produce NPs as small as 100 nm. This method is inexpensive, simple, and capable of manufacturing high-quality NPs.[38,39]

The principal novelty of this project is to use the sage extract which contains a large number of phytochemical components as a green reducing, capping, and stabilizing source to prepare Al_2O_3 NPs and NiO NPs with unique and extraordinary chemical and physical characteristics. Then, these nanomaterials were extensively characterized using various microscopic and spectroscopic methods to confirm the formation of nanoscale particles. The formation of nanocomposite from the presynthesized metal oxide NPs enhanced the efficiency of removing fluoride from contaminated water. Starting fluoride content, contact time, pH, and sorbent dosage as well as the investigation of sorption−desorption kinetics and isothermal processes were all taken into account in the defluoridation of polluted water (Scheme 1).

2. MATERIALS AND METHODS

2.1. Materials and Experimental Method. Alumina NPs (Al_2O_3NPs) were prepared in the laboratory using a green technique mediated by coprecipitation and sage extract. Analytical-grade aluminum nitrate nonahydrate [$Al(NO_3)_3 \cdot 9H_2O$, 99.9%], nickel nitrate hexahydrate [$Ni(NO_3)_2 \cdot 6H_2O$], and sodium hydroxide (98.0%) were supplied by Sigma-Aldrich (Hamburg, Germany). For the environmentally friendly preparation of metal oxide nanostructures, the coprecipitation method is a faster and easier method than others (micro-

https://doi.org/10.1021/acsomega.3c09076
ACS Omega 2024, 9, 23220−23240

Scheme 2. Schematic Illustration for the Preparation Steps of Alumina/NiO Nanocomposite from *S. officinalis* Leaf Extract

emulsion, hydrothermal, and microwave). In this work, deionized water (resistivity > 18.2 M cm) was used. *S. officinalis* leaves were purchased from local markets in Riyadh, Saudi Arabia.

2.2. Preparation of *S. officinalis* Leaf Extract. The *S. officinalis* leaves were cleaned with deionized water and air-dried for 12 h. The dried and cleaned leaves were ground into fine powder for 60 s. Approximately, 25 g of produced *S. officinalis* powder was extracted for 2 h at 80 °C using a deionized water solvent (250 mL) and continual stirring (200 rpm). Following extraction, the mixture was filtered through Whatman filter paper no. 1 and stored in a tight and clean container at 4 °C for future research.[40]

2.3. Biogenic Synthesis of Alumina NPs. At 80 °C for 30 min, the required aluminum nitrate nonahydrate concentration (2.0 mol L^{-1}, 50 mL) and 20 mL of the previously prepared *S. officinalis* leaf extract were mixed with constant stirring. During the next 30 min, a few drops of sodium hydroxide (1.0 mol L^{-1}) were carefully added. The coprecipitated NPs were precipitated overnight. To remove any water moisture, the yellowish precipitate of Al_2O_3 NPs was filtered and air-dried at 100 °C for 12 h. Finally, the formed nanomaterials were crushed into a fine powder and stored in a clean, tightly sealed container for later confirmation and use.[41]

2.4. Biogenic Synthesis of Nickel Oxide NPs. With minor adjustments, the green preparation of NiO NPs followed the previous literature.[42] After 30 min of continuous stirring, 20 mL of *S. officinalis* leaf extract was added to 100 mL of nickel nitrate hexahydrate (2.0 mol L^{-1}). A greenish-colored precipitate was formed. After centrifugation at 2500 rpm for 5 min, the NPs were filtered and stored in the dried and cleaned bottles for further experiments.

S. officinalis extract plays an important part in the synthesis process since it has a high proportion of essential oils due to the presence of glandular structures that are responsible for the creation of volatile oils such as a mixture of monoterpenes and sesquiterpenes as well as triterpenoids. *S. officinalis* also contains bioactive substances, such as salvianolic acids, caffeic acid, carnosol, carnosic acid, rosmarinic acid, cinnamic acid, chlorogenic acid, methyl rosmarinate, and quinic acid. This plant contains flavonoids such as apigenin, quercetin, ferulic acid, and others. During the production of nanomaterials, all of these phytochemical components serve critical roles as natural reducing, capping, and stabilizing materials.[43]

2.5. Grinding Synthesis of Alumina/NiONP Nanocomposites. The alumina/NiO nanocomposite (NCS) was obtained by mixing 1.0 g of the previously prepared alumina and NiO NPs and directly grinding them in a mortar to prepare the nanocomposite. The synthesis procedures are illustrated in Scheme 2.

2.6. Characterization. The shape, crystallite size, and surface morphology were confirmed by various spectroscopic and microscopic techniques. The surface shape and appearance, as well as the elemental composition of the synthesized nanomaterials, were determined using a JEOL scanning electron microscope in conjunction with energy-dispersive X-rays (SEM, JEOL, Tokyo, Japan). An X-ray diffractometer (Thermo Electron, Ecublens, Switzerland) was used to confirm the purity of the formed nanomaterials and their crystalline phases. Transmission electron microscopy (TEM, JEOL-1400, Tokyo, Japan) was also used to study the shape and size of the NPs. Fourier transform infrared (FT-IR, PerkinElmer, Llantrisant, United Kingdom) was used to confirm the functional groups observed on the surface of the nanomaterials during the fabrication process.

2.7. Fluoride Sorbent Experiments. Batch experiments were used to study fluoride adsorption on alumina/NiO NCS at room temperature (25 ± 2 °C). Approximately, 100 mL of

https://doi.org/10.1021/acsomega.3c09076
ACS Omega 2024, 9, 23220−23240

fluoride solution with different initial concentrations (5 to 50 mg/L) was shaken with a predetermined dose of 0.8 g of adsorbent at 150 rpm (Remi CIS4BL orbital shaker). The samples were filtered with Whatman filter paper no. 4, and the filtrate was analyzed for residual fluoride concentration. An indicator, Eriochrome Black T, was added, and the samples were measured at 544 nm using a spectrophotometer (Shimadzu, Kyoto, Japan).

The World Health Organization recommends a fluoride level of 0.5−1 ppm in drinking water.[7] However, the industrial water effluents for dental paste products present in water may elevate up to more than 100 ppm. Therefore, in this study, the calibration graph was plotted covering a wide range from 0.1 to 100 mg/L. To boost the accuracy of the reading, a 1:1 ratio of total ionic strength adjustment buffer solution was employed with the sample solutions for the detection to avoid any interferences present in the analyte solution. The amount of adsorbed fluoride was determined using the following eq 1[44]

$$q_e = \frac{C_0 - C_e}{M} \times V \quad (1)$$

where these values represent q_e (the equilibrium concentration of F ions, mg/g), C_0 and C_e (the initial and equilibrium concentrations), V (the volume of the solution, L), and M (the mass or dosage of the synthesized adsorbent, g/L), respectively. All batch experiments were repeated, and the mean of the values was used as the error bar in the findings and discussion, with the standard deviation acting as the standard deviation.

3. RESULTS AND DISCUSSION

3.1. Sorbent Characterization. To investigate the existence or absence of phytochemicals in *S. officinalis* L., some standard chemical tests were carried out according to the previously reported procedures in the literature.[45−48] These include Dragendroff reagent in the presence of hydrochloric acid for alkaloids, ferric chloride for gallic and catechic tannins, sodium hydroxide for coumarins, foam test for saponin, bromothymol blue for organic acids, sulfuric acid for unsaturated sterol, hydrochloric acid for condensed tannins, Keller Kilian test for glycosides, Libermann Burchard for steroids, and Salkowski's test for terpenoids. The obtained results are summarized in Table 1.

The synthesized alumina NPs, NiO NPs, and alumina/NiO NCS were stabilized by the biogenic active moieties present in *S. officinalis* extract. The FT-IR spectra of *S. officinalis extract* (Figure 1a) revealed various absorption peaks related to the presence of polyphenols, flavonoids, essential oils, and other bioactive molecules. The presence of bands observed at 3751 and 3413 cm^{-1} was due to the existence of strong O−H stretching vibration of phenols, alcohols, and the N−H of amine compounds, respectively; these bands are related to sesquiterpene alcohol and viridiflorol components that are commonly present in *S. officinalis* extract.[49] The bands appeared at 2927 and 2857 cm^{-1} due to the characteristic C−H/CH_2 or CH_3 stretching vibration of aliphatic compounds.[50] The band at 2092 cm^{-1} is related to the strong N═C═S stretching vibration of isocyanate. The bands at 1735 cm^{-1} (strong C═O stretching vibration that can be related to the presence of thujone and camphor), 1619 cm^{-1} (an intermediate C═C stretching vibration of the aromatic ring), 1376 cm^{-1} (an intermediate O−H stretching vibration of the alcohol), 1256 cm^{-1} (a strong C−O stretching vibration of the aromatic ester), and 1058 cm^{-1} (a strong CO−O−CO stretching vibration of the anhydride) are also observed. Furthermore, the band found at 774 cm^{-1} is owing to the presence of trisubstituted strong C−H bending, while the bands at 619 and 481 cm^{-1} are related to the presence of alkyne C−H bending and aryl disulfide (S−S stretching).

Several significant FT-IR bands of alumina NPs (Figure 1b) are observed at 3549, 3472, and 3412 cm^{-1} due to the presence of the O−H stretching of alkyne alcohol and phenols and the medium N−H stretching of primary and secondary amines. However, the bands at 2428 cm^{-1} (S−H stretching of thiol), 2084 cm^{-1} (a strong N═C═S stretching of isothiocyanate), and 1619 cm^{-1} (a strong N−H bending of alkenes, primary amines, and amides) were observed. Furthermore, the absorption bands at 1543 and 1381 cm^{-1}, 1104, 834, and 612 cm^{-1} are due to the presence of a strong N═O stretching of nitro compounds (N−O), a strong C−O stretching of secondary alcohol, a strong C−Cl stretching vibration of the halo compound, and Al−O NPs.[51]

The FT-IR spectrum of NiO NPs (Figure 1c) shows different absorption bands at 3429, 2362, 1635, 1468, and 1379 cm^{-1} due to the existence of a strong broad O−H starching vibration of alcohol, a strong O═C═O starching vibration of carbon dioxide, a medium C═C stretching vibration of alkene, a medium C−H bending vibration of alkane, and a medium C−H bending of aldehyde, respectively. In addition, the bands at 1103 and 986 cm^{-1} are related to a strong C−O starching of second alcohol and a strong C═C bending vibration of alkene, respectively. The bands at 660 and 619 cm^{-1} are due to a strong halo compound, and the band at 469 cm^{-1} is for Ni−O NPs.[52]

Moreover, the bioactive compounds such as polyphenols, flavonoids, alkaloids, essential oils, and others present in the *S. officinalis* extract act as bioreducing capping and stabilizing natural materials for the alumina/NiO nanocomposite. The FT-IR spectrum (Figure 1d) shows the presence of various functional groups expressed by 3412 cm^{-1} (medium N−H stretching of primary amine), 2428 cm^{-1} (strong O═C═O stretching of carbon dioxide), 1633 cm^{-1} (medium C═C stretching of the aromatic ring), 1470 and 1375 cm^{-1} (medium C−H bending of proteins), 1100 cm^{-1} (strong C−O stretching of secondary alcohol), 986 cm^{-1} (strong N−H of primary and secondary amines), 657 and 620 cm^{-1} (strong C−Cl halo compound), and 463 cm^{-1} (Al−O and Ni−O NPs).[53]

TEM was used to investigate the surface shape of the synthesized alumina NPs, NiO NPs, and alumina/NiO NCS. The images were picked at magnifications of 250 000, 150 000, and 150 000 for the above nanomaterials, respectively. It was

Table 1. Qualitative Assay for Preliminary Phytochemical *S. officinalis* Extract

phytochemicals	chemical test	positive indication sign
alkaloids	Dragendroff reagent[45]	orange or red precipitate
steroids	Libermann Brachard[45]	red color
gallic tannins	ferric chloride (1%)[46]	blackish blue color
catechic tannins	ferric chloride (1%)[46]	greenish color
coumarins	sodium hydroxide[46]	yellow fluorescence
unsaturated sterols	sulfuric acid[46]	red color
organic acids	bromothymol blue[46]	canary yellow
condensed tannins	hydrochloric acid[46]	red color
saponin	foam test[47]	foam more than 1 cm
terpenoids	Salkowski's test[47]	reddish-brown precipitate
glycosides	Keller Kilian test[48]	red color

https://doi.org/10.1021/acsomega.3c09076
ACS Omega 2024, 9, 23220−23240

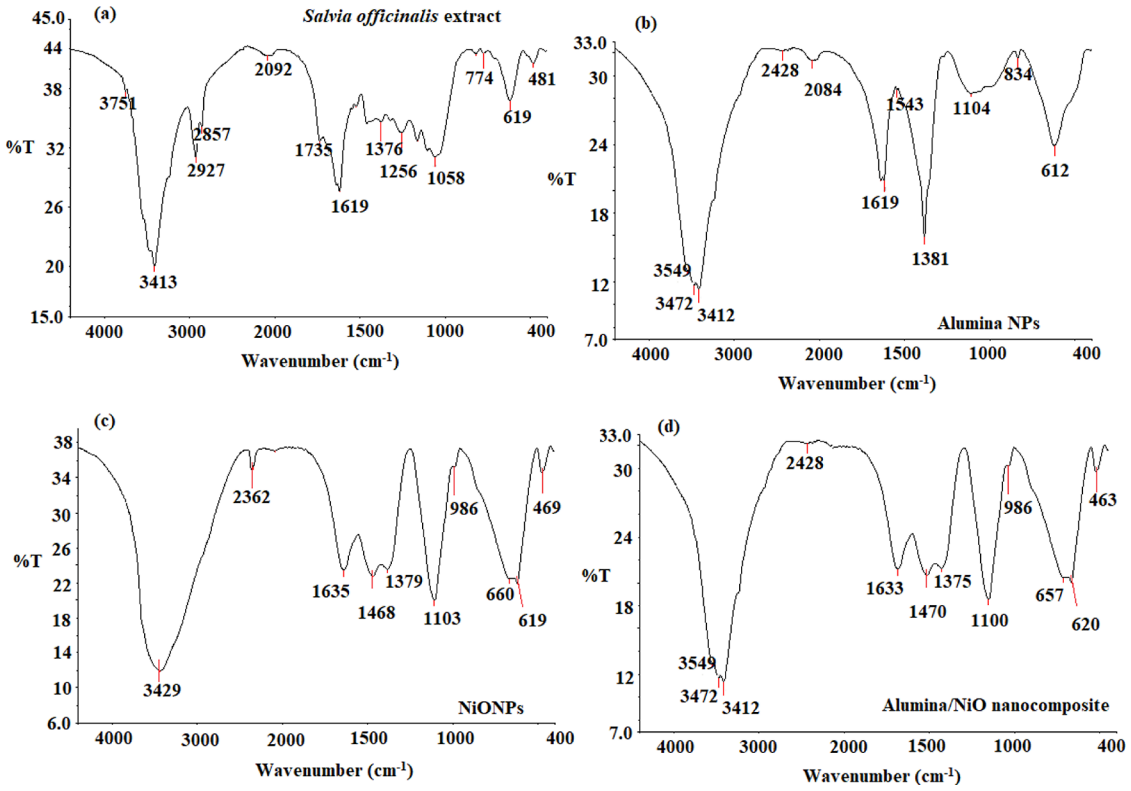

Figure 1. FT-IR analysis of (a) *S. officinalis,* (b) alumina NPs, (c) NiO NPs, and (d) alumina/NiO NCS measured at 4000−400 cm^{-1}.

observed that a majority of the NPs are spherical and well dispersed. The average particle sizes for the three nanomaterials are 25 ± 1.2, 27 ± 1.1, and 35 ± 1.6 nm for alumina NPs, NiO NPs, and alumina/NiO NCS, respectively (Figure 2a−c).

The surface morphologies of alumina NPs, NiO NPs, and alumina/NiO NCS were studied using scanning electron microscopy (SEM)/atomic force microscopy (AFM) 3D images at a magnification of 50 000× for nanoscale materials. The microscopic images of the studied alumina NPs and NiO NPs samples show spherical particles with remarkable pores and an average particle size of around 35 nm (Figure 3a−c) TEM and SEM show that the majority of the NPs are spherical in shape with an average particle size of around 35 nm. AFM images show a good distribution and size between 20 and 60 nm.

A scanning electron microscope connected with an energy-dispersive X-ray (EDX) spectrometer was used to investigate the elemental composition of the green synthesized metal oxide nanomaterials (alumina NPs, NiO NPs, and alumina/NiO NCS). According to the findings, the weight and atomic % were found for Al (26.47 and 17.61%) and for O (73.51 and 82.39%), respectively. For NiO NPs, the weight and atomic % were Ni (54.88 and 24.89%) and O (45.12 and 75.11%), respectively. Meanwhile, the EDX spectrum of alumina/NiO NCS showed weight and atomic % of O (49.22 and 62.77%), Ni (34.43 and 32.96%), and Al (16.35 and 4.27%), respectively (Figure 4a−c).

Mapping in X-ray microanalysis refers to the accumulation and evaluation of X-ray spectra point by point to identify the concentration of particular preset chemical components. Each elemental map produced reflects the two-dimensional concentration distribution of the corresponding element throughout the sample surface.[54] The elemental mapping results show that the alumina NPs, NiO NPs, and alumina/NiO NCS were successfully formed (Figure 5a−c).

To identify and determine diverse crystalline structures in materials, analytical methods such as X-ray diffraction (XRD) are utilized. This investigation was carried out with the aid of a Cu-k XRD diffractometer (k = 1.5406 Å). The XRD diffraction study of alumina NPs (Figure 6a) shows remarkable diffraction peaks at 2θ values of 22.93, 29.49, 32.51, 38.99, 46.52, 62.45, 67.21, 86.73, and 87.41° corresponding to (1 1 4), (0 1 2), (2 2 0), (1 1 0), (4 0 0), (4 2 2), (4 4 0), (3 0 0), and (6 2 0) face-centered cubic of alumina. These peaks are matched with those of alumina obtained from JCPDS Card no. 79-1558.[55]

The NiONPs XRD spectrum (Figure 6b) revealed strong and distinct peaks at 2θ = 37.20, 43.20, 62.87, 75.18, and 79.22° that correspond to (1 1 1), (2 0 0), (2 2 0), (3 1 1), and (2 2 2) crystalline planes, respectively. These NiONP diffraction measurements corroborated the formation of a spherical crystalline phase of NiO and corresponded to the JCPDS map of NiO 04-0835.[56]

Different significant peaks were found in the alumina/NiO NCS XRD spectrum (Figure 6c), indicating the existence of alumina NPs and NiO NPs, validating the creation of the nanocomposite.

However, Debye−Scherrer's eq 2[57] was used to calculate the average crystallite size of green-synthesized alumina NPs, NiO NPs, and alumina/NiO NCS.

$$D = (0.94\lambda/\beta \cos\theta) \quad (2)$$

These values represent D (the particle size nm), 0.94 (constant), λ (X-ray light wavelength with value 1.54 × 10^{-10}), β (full width at half-maximum, fwhm), and θ (Bragg angle, degree), respectively. The calculated average crystallite sizes of alumina NPs, NiO NPs, and alumina/NiO NCS were determined to be 19.14 ± 2.4, 17.7 ± 2.1, and 20.64 ± 2.6 nm, respectively.

https://doi.org/10.1021/acsomega.3c09076
ACS Omega 2024, 9, 23220−23240

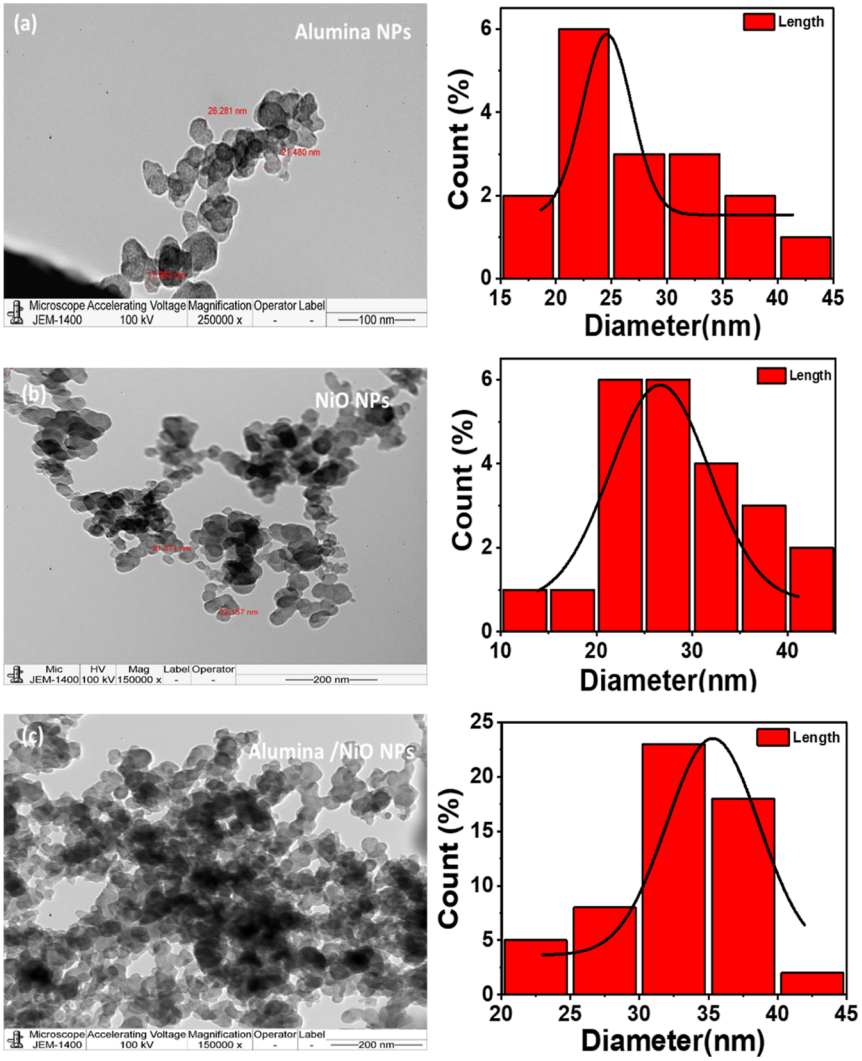

Figure 2. TEM images with a J-image of particle size of (a) alumina NPs, (b) NiO NPs, and (c) alumina/NiO NCS.

The chemical states of alumina and NiO NPs were characterized by X-ray photoelectron spectroscopy (XPS). The Al 2p spectra were split into a metallic and an oxide component by fitting in the binding energy ranges of 70−80 eV. The fitted spectra show the presence of an oxide peak at a binding energy of 76.36 eV (Figure 7a). The O(1s) region in (Figure 7b) shows a peak at 534.50 eV attributed to oxygen in Al_2O_3 and another peak at 532.3 eV attributed to oxygen in combination with the OH^- in aluminum hydroxide.[58]

In contrast, for the NiO NPs, the Ni 2p region, the 2p3/2 main peak, and its satellite are at 858.99 and 862.07 eV, and the Ni 2p1/2 main peak and its satellite are at 865.85 and 876.68 eV, respectively (Figure 7d). The O(1s) region is attributed to the surface hydroxyl groups at 535.51 eV and two peaks originating from the lattice oxygen at 534.09 eV and adsorbed water at 536.29 eV (Figure 7e).[59]

The characteristic of the C 1s region of the alcohol type (C−OH) ∼ 286 eV, carboxyl (C═O) ∼ 288 eV, and carbonate (O−C═O) ∼ 290 eV is observed (Figure 7c,f).

3.1.1. Surface Area and Pore Diameter. The Barret−Joyner−Halenda (BJH) pore size distribution diagrams of alumina NPs, NiO NPs, and alumina/NiO NCS were examined in conjunction with the N_2 adsorption/desorption isotherms. At a relative pressure (P/P_0) in the range of 0.1−1.0, the three samples exhibit a typical IV pattern of the IUPAC isotherm type with a prominent hysteresis loop, where a narrow hysteresis loop in the low-pressure area suggested the existence of open-structured mesopores (Figure 8a−c).

The Brunauer−Emmett−Teller (BET) method was used to analyze surface area, and the results showed that for alumina NPs, NiO NPs, and alumina/NiO NCS, respectively, the surface areas were 148.4 ± 0.7, 128.5 ± 0.2, and 187.6 ± 0.3 $m^2\ g^{-1}$ with pore volumes of 0.49, 0.62, and 0.86 $cm^3\ g^{-1}$. The total pore volume of the nanocomposite sample was found to have increased, suggesting that the two metal oxides were used to improve the morphological structure of the nanocomposite by increasing the specific surface area and pore volume of alumina/NiO NCS.

3.2. Factors Influencing Adsorption Potential. *3.2.1. Effect of Sorbent Dose.* The effects of the presynthesized adsorbents alumina NPs, NiO NPs, and alumina/NiO NCS on the adsorption of F^- ions were studied with adsorbent dosages of 0.1−2 g/L. Figure 9a shows the percent elimination of the F^- ions. The percent removal of F^- ions increases dramatically with adsorbent dose, which can be attributed to an increase in the number of active sites.[60] Adsorption was found to be uniform at adsorbent doses greater than 0.8 g/L. Consequently, an adsorbent dose of 0.8 g/L was established as

https://doi.org/10.1021/acsomega.3c09076
ACS Omega 2024, 9, 23220−23240

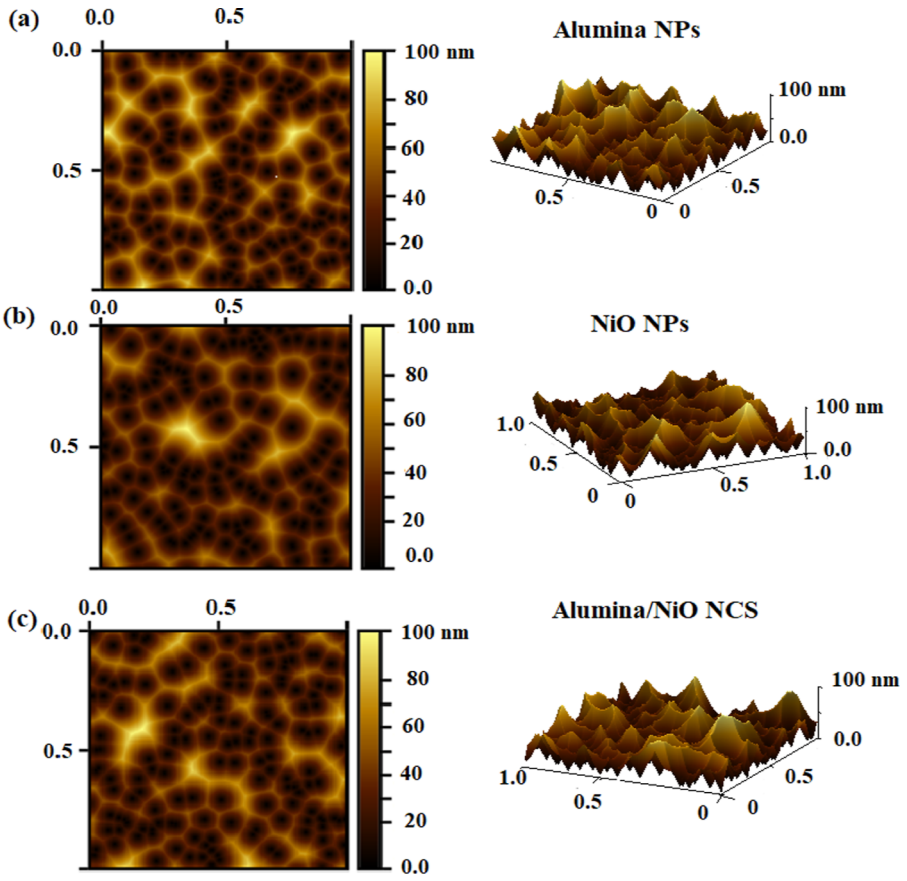

Figure 3. SEM/AFM micrographs of (a) alumina NPs, (b) NiO NPs, and (c) alumina/NiO NCS measured at a magnification of 50 000× magnification.

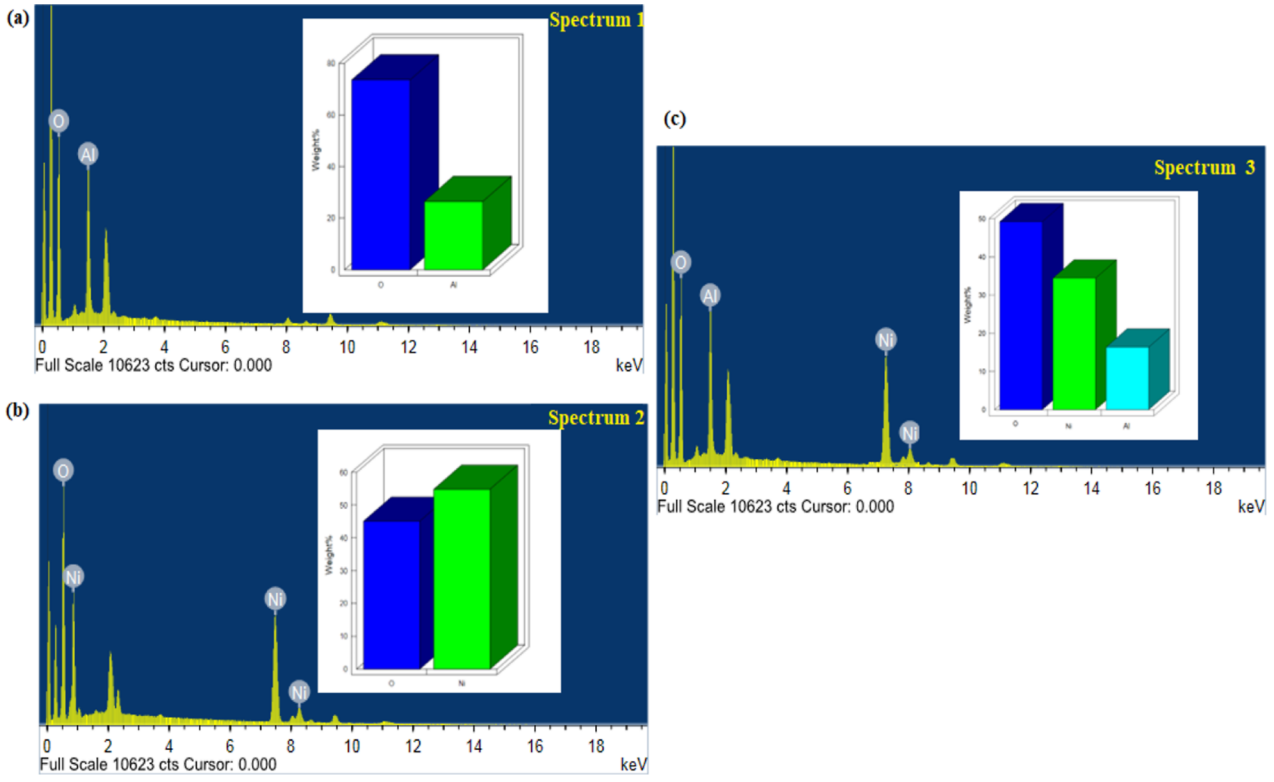

Figure 4. EDX analysis of (a) alumina NPs, (b) NiO NPs, and (c) alumina/NiO NCS synthesized using *S. officinalis* extract.

https://doi.org/10.1021/acsomega.3c09076
ACS Omega 2024, 9, 23220−23240

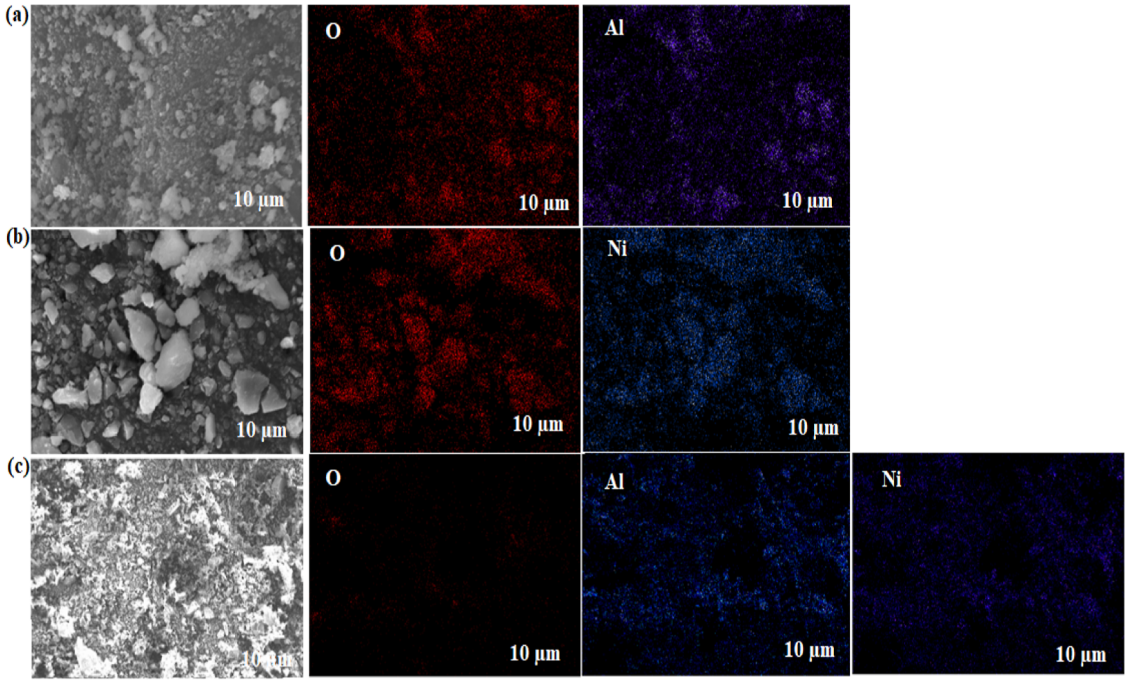

Figure 5. Mapping of (a) alumina NPs, (b) NiO NPs, and (c) alumina/NiO NCS synthesized using *S. officinalis* extract.

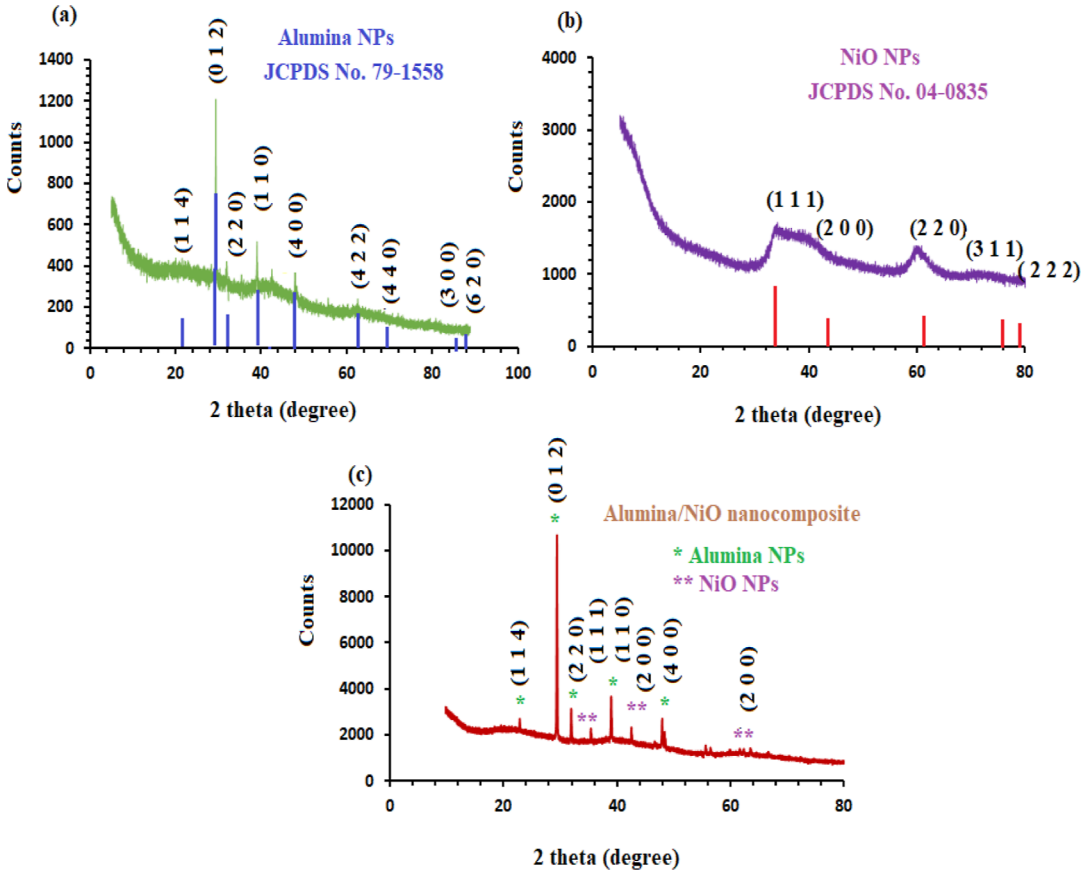

Figure 6. XRD patterns of (a) alumina NPs, (b) NiO NPs, and (c) alumina/NiO NCS.

the optimal dose for generally acceptable F^- ion removal efficiency in all future experiments. When alumina NPs, NiO NPs, and alumina/NiO NCS were compared, the nanocomposite was found to be more efficient than alumina or NiO NPs in removing F^- ions from water.

3.2.2. Effect of Contact Time. Contact time is an important parameter because it influences sorbate kinetics at a given starting concentration.[61] Using an equilibrium dose of alumina NPs, NiO NPs, and alumina/NiO NCS, the impact of contact time was investigated by varying the time period from 0 to 360

https://doi.org/10.1021/acsomega.3c09076
ACS Omega 2024, 9, 23220−23240

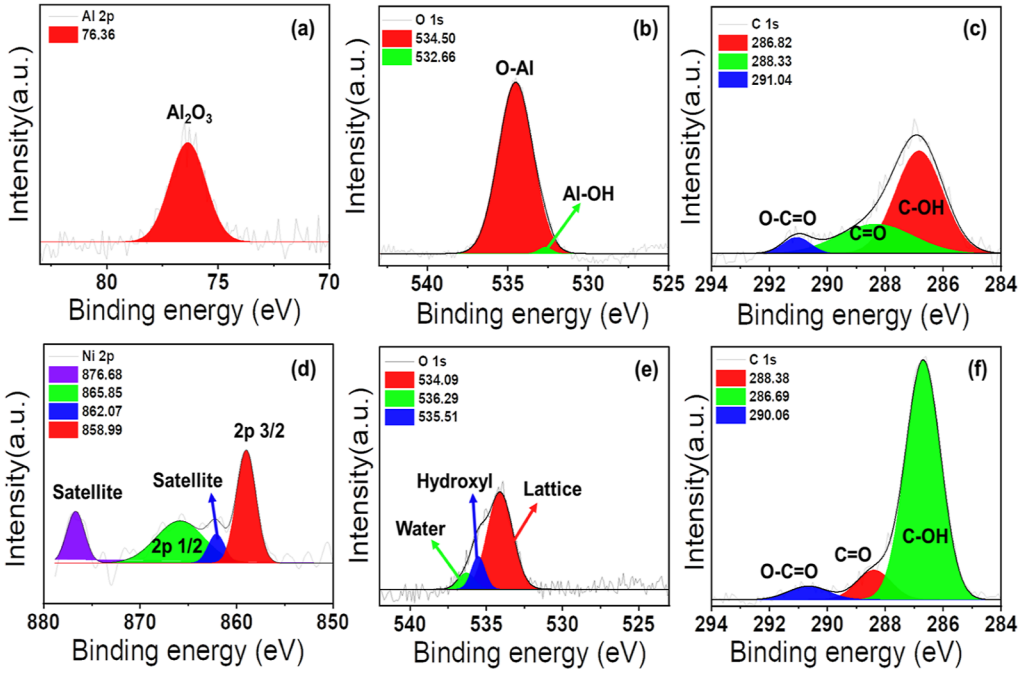

Figure 7. Binding energy of (a) Al 2p, (b) O 1s, (c) C 1s for alumina NPs, (d) Ni 2p, (e) O 1s, and (f) C 1s for NiO NPs.

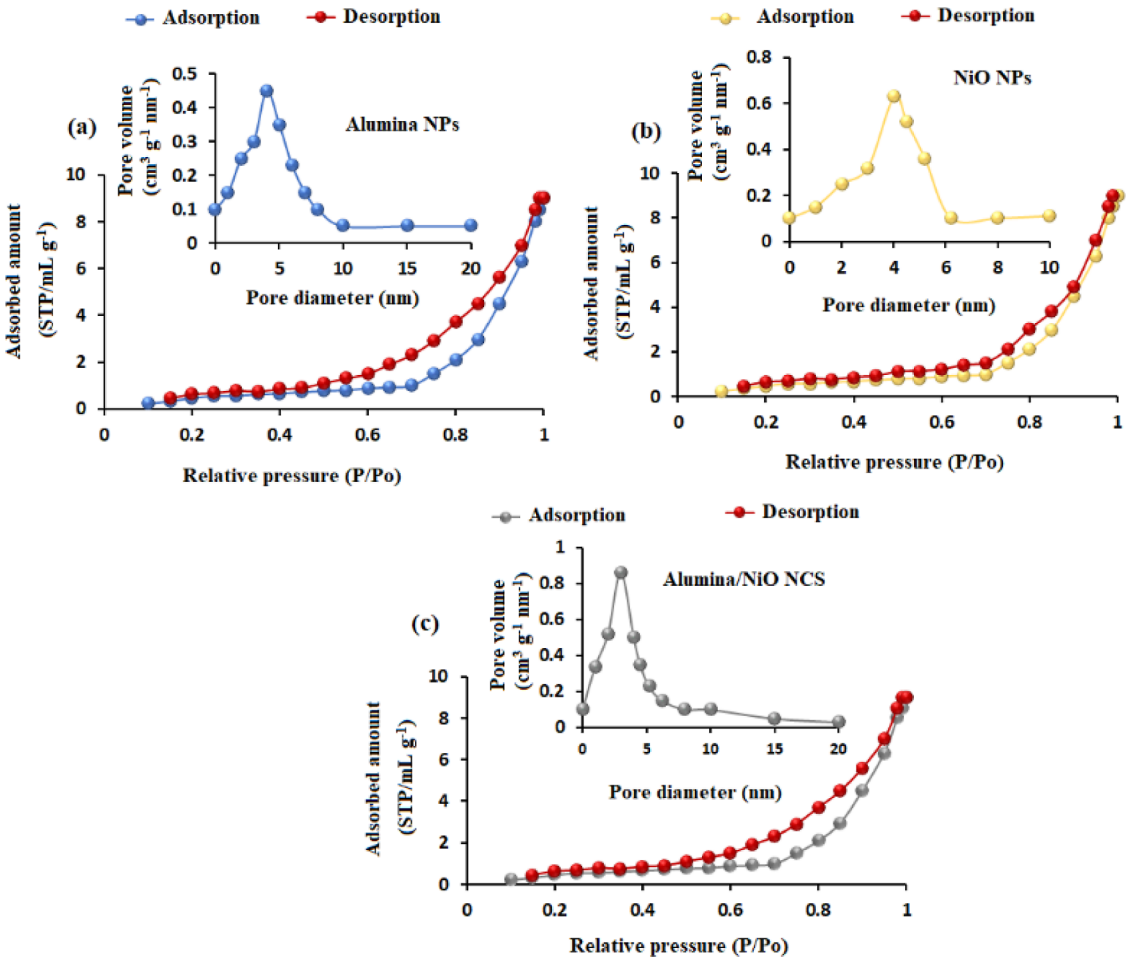

Figure 8. BET/BJH surface area and pore distribution analyses for (a) alumina NPs, (b) NiO NPs, and (c) alumina/NiO NCS.

min. Figure 9b depicts the fast adsorption of F ions in 90 min. After that, the process slows down and approaches equilibrium after 120 min. Adsorption did not increase much (less than 1%) as the contact time was increased up to 6 h, indicating that

https://doi.org/10.1021/acsomega.3c09076
ACS Omega 2024, 9, 23220−23240

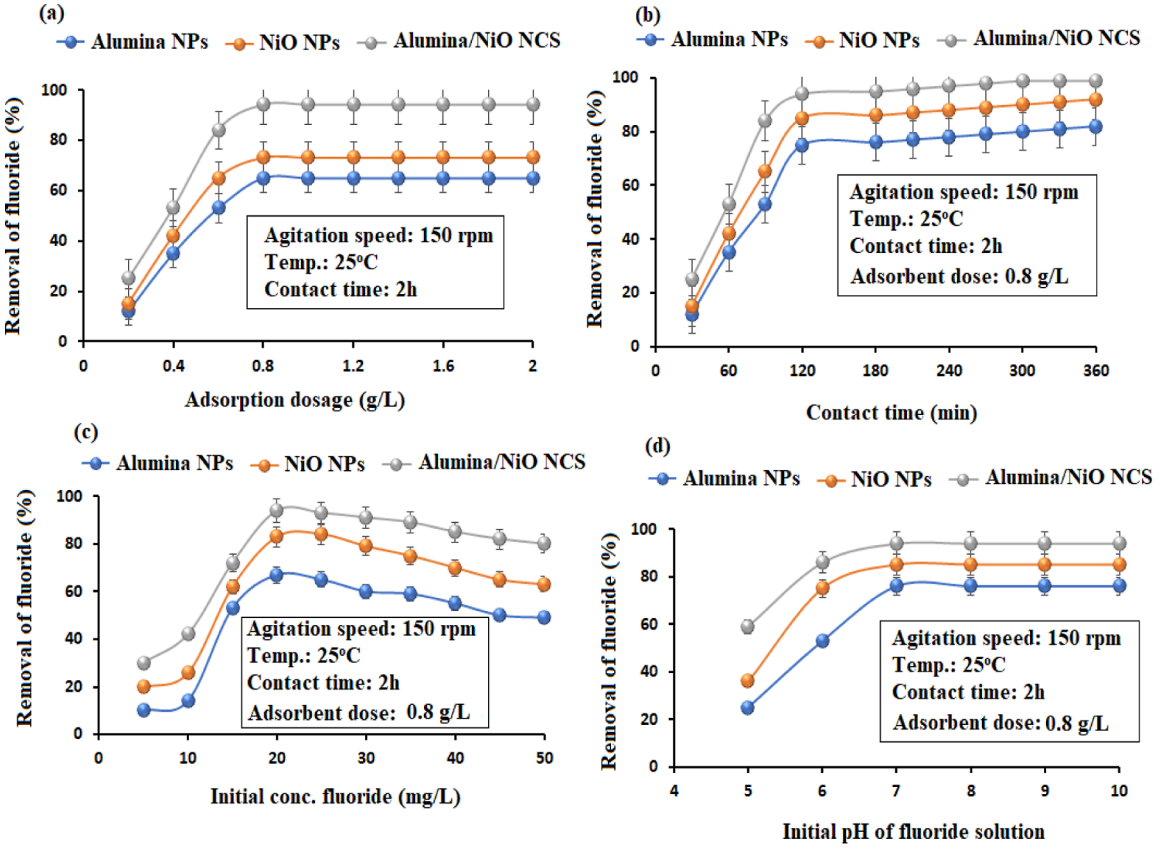

Figure 9. Optimization conditions of adsorption efficiency under the effect of (a) adsorption dosage (g/L), (b) contact time (min), (c) initial concentration of fluoride solution (mg/L), and (d) initial pH of fluoride solution in the range of 5−10.

adsorption may be finished within 2 h. As a result, more investigations were conducted during a 2 h period.

3.2.3. Effect of Initial Fluoride Concentration. To determine the effect of initial F concentration on adsorption quantity, 0.8 g/L alumina NPs, NiO NPs, and alumina/NiO NCS was dispersed individually in 5−50 mg/L fluoride solution for 2 h. Figure 9c depicts the findings. According to reports, the adsorption rate is quick initially and subsequently slows down as the fluoride concentration increases. As fluoride concentration rises, so does competition for active adsorption sites, and the adsorption process slows.[62] The adsorption capability of alumina/NiO NCS is greater than that of alumina NPs or NiO NPs. This is because alumina/NiO NCs have a surface area/volume ratio that is higher than that of individual NPs. In subsequent trials, the appropriate starting fluoride concentration was 20 mg/L.

3.2.4. Effect of Initial pH Values and Sorption Mechanism. The pH of the medium has a significant effect on the adsorption process, and experiments were conducted with a pH range of 5−10 (Figure 9d) at a constant fluoride content of 20 mg/L. At a pH of 7, all nanomaterials eliminated the maximum percentage of fluoride. The 2% improvement in fluoride removal up to pH 7 is due to alumina's positively charged surface attracting negatively charged fluoride ions up to pH 7, which is lower than its pH_{pzc}. Owusu-Agyeman et al. (2017) state that[63] fluoride ions altered when the pH of the medium changed. F^- ions react with H^+ ions at extremely low pH to form HF^{2-}, HF, H_2F_2, and other species, and the concentration of these species in the aqueous medium is indicated by their thermodynamic equilibrium constants (pK_a), according to George et al., 2010.[64] At acidic pH, F^- is present mainly (90%) as HF, although it dissociates to F^- at a pK_a of 3.2. When the pH of a solution altered from neutral to acidic, the concentration of hydrogen ions increases and HF acid is produced, which is no longer accessible for adsorption and diminishes adsorption capacity. At pH more than 6.0, fluoride ion quantities represent about 100% of the total fluoride in aqueous medium.[65] Above pH 7, the adsorption capacity is reduced, which might be attributed to hydroxyl ions competing for active sites in the solution. Furthermore, the adsorbent surface becomes negatively charged and repels fluoride anions.[66] At pH 7, the percentage removal of F^- ions was estimated under constant experimental conditions (adsorbent dosage of 0.8 g/L), a contact time of 2 h, a temperature of 25 °C, and initial F^- concentrations of 20 mg/L to be 67, 85, and 94% for alumina NPs, NiO NPs, and alumina/NiO NCS, respectively.

The distribution coefficient K_D is a parameter that may be used to evaluate the affinity of the adsorbent surface for an element and can be computed using the following eq 3[67]

$$K_D = \frac{C_s}{C_w} \tag{3}$$

where C_s and C_w represent the concentration of fluoride in the adsorbent (mg/g) and the residual fluoride concentration (mg/L), respectively. Figure 10a shows the obtained K_D values as a function of pH. It is critical to remember that the higher the K_D value, the better the binding capability of the target pollutant.[68]

The surface charge of the adsorbent is zero at the point of zero charge (pH_{zpc}). The surface charges of alumina NPs or NiO NPs generated from aluminum or nickel oxide and alumina/NiO

https://doi.org/10.1021/acsomega.3c09076
ACS Omega 2024, 9, 23220−23240

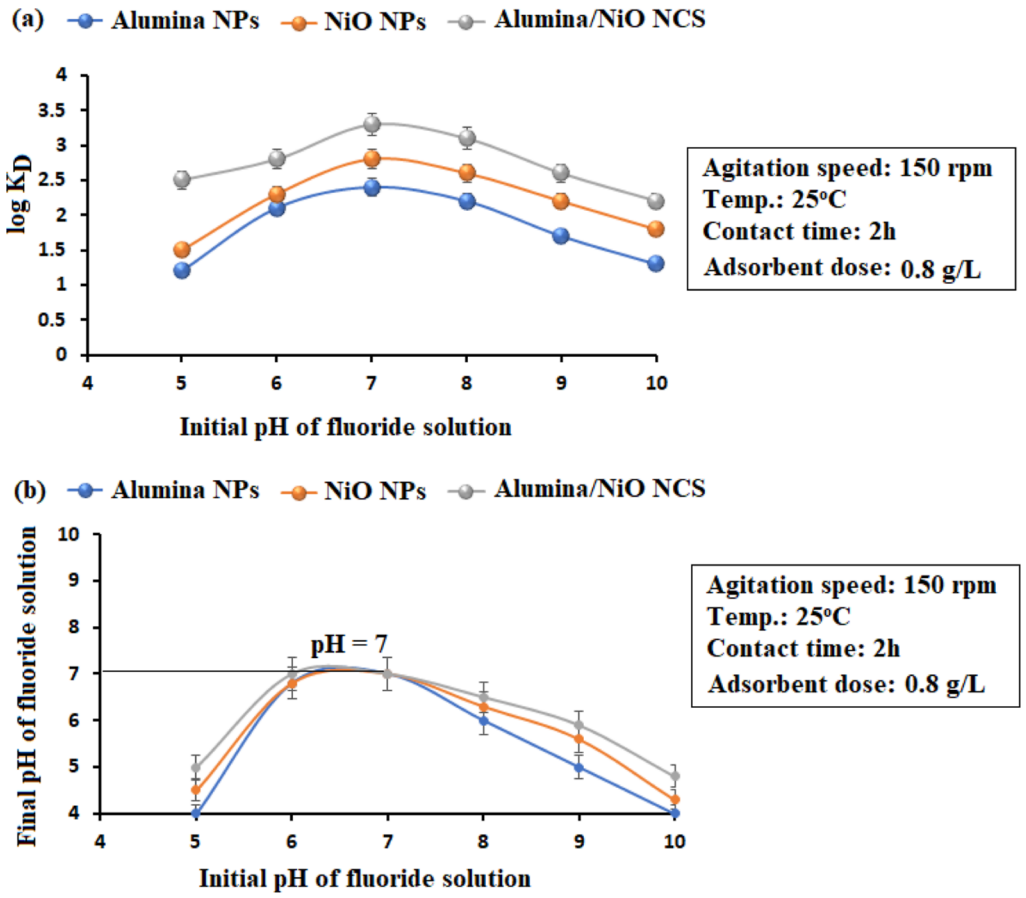

Figure 10. (a) Graph of initial pH of fluoride solution (20 mg/L) vs log K_D and (b) graph of initial pH of fluoride solution (20 mg/L) vs final pH of fluoride solution using alumina NPs, NiO NPs, and alumina/NiO NCS.

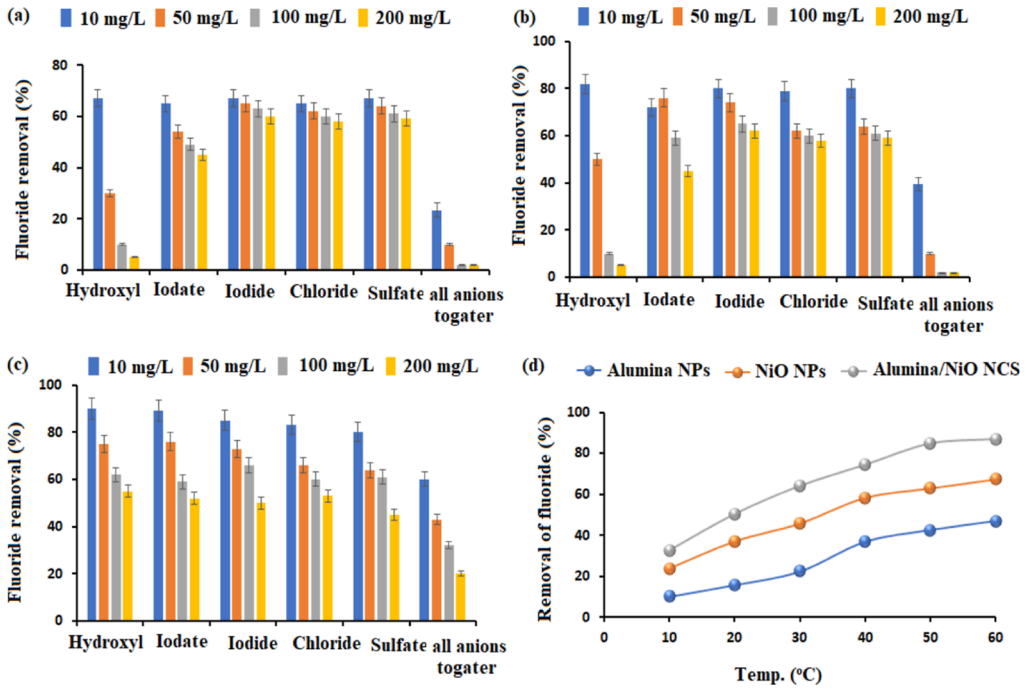

Figure 11. Removal % of fluoride in the presence of various anions with different concentrations of 10, 50, 100, and 200 mg/L in the presence of (a) alumina NPs, (b) NiO NPs, and (c) alumina/NiO NCS. (d) The influence of temperature on the removal % of fluoride.

NCS are measured by the pH_{pzc} of the adsorbent and the isoelectric point of the aqueous medium in the presence of fluoride ions. The pH_{Pzc} of the synthesized nanomaterials is 6.8 ± 0.1 demonstrating that below this pH value, the surface charge

https://doi.org/10.1021/acsomega.3c09076
ACS Omega 2024, 9, 23220−23240

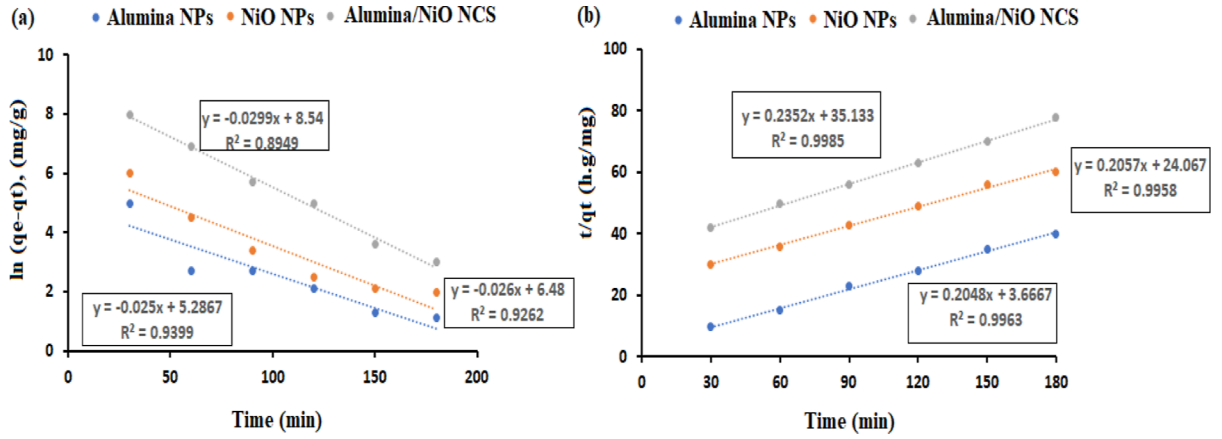

Figure 12. Kinetic plots of (a) pseudo-first order, values q_e and q_t (mg/g), and (b) pseudo-second order for the fluoride ion removal using alumina NPs, NiO NPs, and alumina/NiO NCS.

of the nanomaterials is positive and above this pH value, it is negative. It can be noticed that above pH 6.8, there is strong electrostatic repulsion between fluoride ions and the negatively charged nanomaterials. The following mechanisms can explain fluoride adsorption between the pH ranges of 2−10. At pH less than pH_{zpc}, the adsorption mechanism is primarily electrostatic/Coulombic attraction or the anion-exchange reaction. Because of variations in the availability of positive charge surface, the adsorption capacity drops in the pH range of 3.5−5 (below pH_{zpc} value), suggesting that the adsorption mechanism now follows the ion-exchange process between positively charged adsorbents and the negatively charged fluoride ions. Adsorption capacity is reported to decrease dramatically at pH values higher than pH_{zpc}. This is due to the fact that at pH greater than pH_{zpc}, the adsorbent's surface is effectively negatively charged, resulting in repulsion between the negatively charged binary oxide nano adsorbent surface and the negatively charged fluoride anion. At higher pH, the abundantly available OH^- and F^- compete for active adsorption sites, resulting in lower adsorption capacity. The results reveal that alumina NPs, NiO NPs, and alumina/NiO NCS are all effective at eliminating F^- ions from water samples. It is also highlighted that the K_D versus pH plots of alumina/NiO NCS increase considerably with increasing pH, suggesting that NCS is more pH-sensitive than alumina NPs and NiO NPs. The variation in absorbance with regard to the original pH of the solution can be explained by the adsorbent's zero-point charge. A plot of the beginning pH of the fluoride working solution vs the end solution pH was used to determine the zero point of alumina NP, NiO NPs, and alumina/NiO NCS. The results reveal that at pH 7, alumina NP, NiO NPs, and alumina/NiO NCS have the same zero-point charge. Furthermore, at 25 °C, the adsorbent's greatest sorption capacity was determined to be 2.4, 2.8, and 3.3 mg/g, respectively (Figure 10a,b).

3.2.5. Effect of Competing Anions. The influence of co-ions in contaminated water such as iodide, iodate, chloride, sulfate, and hydroxide on defluoridation capability was investigated. The anion concentrations were varied 10, 50, 100, and 200 mg/L, whereas the fluoride content remained constant at 20 mg/L at room temperature. As shown in Figure 11a−c, the removal efficiency of F^- ions was calculated using alumina NPs, NiO NPs, and alumina/NiO NCS adsorbents in the presence of other competing anions at pH 7 and constant adsorption conditions (150 rpm agitation speed, 25 °C temperature, and contact time 2 h). The adsorption capacity was found to decrease significantly with an increase in the concentration of these competing anions. It might be due to competition for locations on the sorbent surfaces, which is determined by the concentration, charge, and size of the anions. Fluoride adsorption by alumina NPs, NiO NPs, and alumina/NiO NCS adsorbents is significantly affected by the presence of competing anions such as hydroxide ions. Fluoride removal reduces in the alkaline pH range due to hydroxyl ions competing for active sites in the solution. The amounts of competing anions in this investigation were far greater than those found in groundwater. Thus, even at extremely high concentrations of the competing anions utilized in this work, alumina NPs, NiO NPs, and alumina/NiO NCS adsorbents were able to remove fluoride from drinking water at pH ranging from 3.5 to 7. These results are in agreement with those obtained in the previously reported study.[69]

3.2.6. Effect of Different Temperatures. Temperature affects the adsorption process in two ways. As the viscosity of the solution decreases, it is known that an increase in the temperature increases the rate of diffusion of adsorbed molecules through the outer boundary layer and the inner pores of the adsorbent particles. Moreover, temperature changes the equilibrium capacity of the adsorbent for a given adsorbate.[70] Figure 11d shows the effect of temperature on fluoride removal by alumina NPs, NiO NPs, and alumina/NiO NCS. The graph shows that as the temperature increases, the amount of adsorbed fluoride ions increases. By increasing the temperature from 10 to 60 °C, the percentage of fluoride elimination increases dramatically to 46.9, 67.4, and 86.7% for the above-mentioned nanomaterials, respectively. The outcome suggests that the reaction is endothermic. Temperature increases the mobility of fluoride ions as well as produces a swelling effect inside the internal structure of nanomaterials, allowing fluoride ions to penetrate farther.[71] Consequently, the adsorption capacity should be mainly determined by the chemical interaction between the functional groups on the surface of the nanomaterials and the fluoride ions and should increase with increasing temperature. Since diffusion is an endothermic process, this can be explained by an increase in the diffusion rate of the fluoride ions into the pores.[72]

3.3. Adsorption Kinetics. Adsorption kinetic models are critical for understanding the relationship among adsorption time, concentration, and equilibrium adsorption capacity. The following pseudo-first-order eq 4[73] may be used to understand

https://doi.org/10.1021/acsomega.3c09076
ACS Omega 2024, 9, 23220−23240

Table 2. Adsorption Isotherm Parameters Using Langmuir and Freundlich Isotherms for the Adsorption of Fluoride Ions on the Surfaces of Alumina NPs and FA-Alumina/CuONPs

		Langmuir isotherm				Freundlich isotherm		
S. no.	adsorbents	Q_{max} (mg/g)	K_L (L/mg)	R_L (L/mg)	R^2	K_F (mg/g)	$1/n$	R^2
1	alumina NPs	12.53	5.764	0.0178	0.9975	2.006	1.3187	0.9925
2	NiO NPs	11.49	1.466	0.0329	0.9910	3.709	0.9528	0.9952
2	alumina/NiO NCS	16.58	2.201	0.0222	0.9974	1.186	2.4946	0.9376

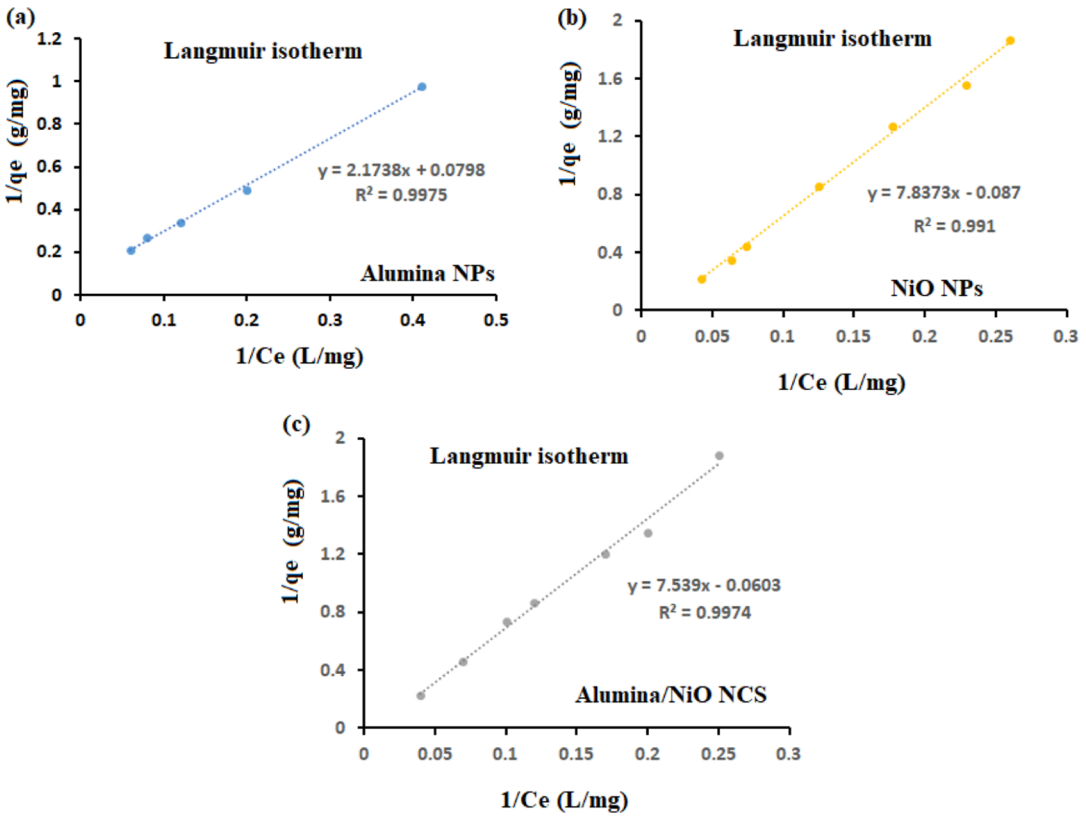

Figure 13. Langmuir adsorption isotherm of fluoride ions on the surfaces of (a) alumina NPs, (b) NiO NPs, and (c) alumina/NiO NCS.

the control stages of the adsorption rate of alumina NPs, NiO NPs, and alumina/NiO NCS

$$\ln(q_e - q_t) = \ln q_e - K_1 t \quad (4)$$

The kinetic of fluoride adsorption on the surface of alumina NPs, NiO NPs, and alumina/NiO NCS was also studied using eq 5[74] of pseudo-second order.

$$\frac{t}{q_t} = \frac{1}{k_2 \times q_e^2} + \frac{1}{q_e} \times t \quad (5)$$

The values q_e (mg/g) and q_t (mg/g) represent the adsorption capacity of alumina NPs, NiO NPs, and alumina/NiO NCS on F^- at adsorption equilibrium and at a specific time point. Meanwhile, the K_1 (h^{-1}) and K_2 (g/mg·h) represent the first-order pseudorate constant and the pseudo second-order rate constant.[75]

The linear graphs of the kinetics models based on pseudo-first order $\ln(q_e - q_t)$ and pseudo-second order $\frac{t}{q_t}$ vs time are shown in Figure 12a,b.

The intercepts and slopes were used to calculate the kinetic parameters of the adsorption of F^- ions on the surface of alumina NPs, NiO NPs, and alumina/NiO NCS. The kinetics of fluoride adsorption onto nanomaterials were studied using two models: pseudo-first order and pseudo-second order. Table 2 summarizes the parameters that were computed. The best-fit model was chosen from the three based on the correlation coefficient (R^2)[76] and numerical agreement between the experimental and computed q_e values. According to the results, the pseudo-second-order kinetic model for the above sorbents better explains the experimental data. The adsorption capacities were found to be 40.15, 60.32, and 78.29 mg/g for alumina NPs, NiO NPs, and alumina/NiO NCS, respectively. Moreover, these results are confirmed by the correlation coefficients R^2, which have values of 0.9963, 0.9958, and 0.9985, all close to 1.

3.4. Adsorption Isotherms. Adsorption isotherms are essential for understanding the adsorption system between the adsorbate and the adsorbent.[77] To further understand the interaction among F^-, alumina NPs, NiO NPs, and alumina/NiO NCS in the adsorption process, Langmuir and Freundlich isotherm models were created to assess the adsorption data. The study was conducted by applying the following formulas:

Formula 6 represents the Langmuir adsorption isotherm model[78]

https://doi.org/10.1021/acsomega.3c09076
ACS Omega 2024, 9, 23220−23240

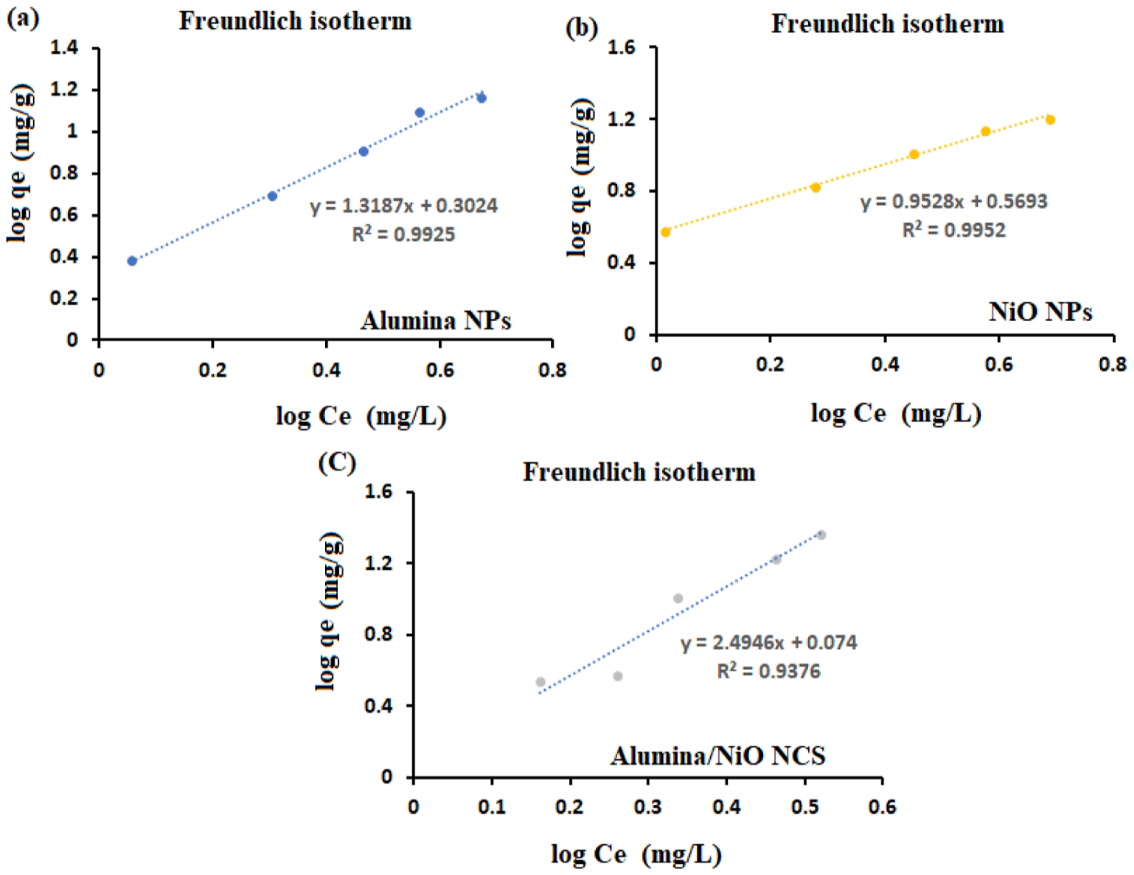

Figure 14. Freundlich adsorption isotherm of fluoride ions on the surfaces of (a) alumina NPs, (b) NiO NPs, and (c) alumina/NiO NCS.

$$\frac{C_e}{q_e} = \frac{C_e}{Q_m} + \frac{1}{Q_m K} \tag{6}$$

Another parameter, R_L, can explain the adsorption according to Langmuir as eq 7

$$R_L = 1/(1 + K_L \times C_0) \tag{7}$$

Based on the R_L value, the adsorption is favorable when R_L tends to zero ($R_L \rightarrow 0$) or unfavorable when R_L tends to one ($R_L \rightarrow 1$). Formula 8 represents the Freundlich adsorption isotherm model[79]

$$\log q_e = \log K_F + \frac{1}{n}\log C_e \tag{8}$$

where C_e (mg/L), Q_e and Q_m (mg/g), and K (L/mg) are the equilibrium concentration of fluoride ions, the adsorption capacity and saturation adsorption capacity, and the Langmuir constant, respectively. K_F (L/mg) is a constant that might represent the saturated adsorption quantity in the Freundlich adsorption isotherm model; and $1/n$ is an empirical parameter that reflects the adsorption intensity. Adsorption intensity changes with material heterogeneity in the Freundlich adsorption isotherm model.[80] The adsorption isotherm model is widely used to study the adsorption mechanism throughout the sorption process. The adsorption effect is strongly influenced by the temperature of the adsorption environment. Langmuir model fitted plots are more similar to experimental graphs than the Freundlich adsorption isotherm model. Table 2 summarizes the obtained data. The slope and intercept of the linear graphs were computed (Figure 13a–c). For alumina, NiO NPs, and alumina/NiO NCS, the values of Q_{max} were found to be (12.53, 11.49, and 16.58 mg/g) constant K_L (2.764, 1.466, and 2.202 L/mg), and R_L (0.0178, 0.0135, and 0.022 L/mg) was obtained. Correlation regression coefficients for the two adsorbents were 0.9975, 0.9910, and 0.9974, respectively. The greater the value of the Langmuir correlation coefficient, the better the Langmuir isotherm model matches the adsorption of fluoride ions on the surface of alumina NPs, NiO NPs, and alumina/NiO NCS, respectively.

For the Freundlich adsorption isotherm model, for alumina NPs, NiO NPs, and alumina/NiO NCS, the values of K_F were found to be (2.006, 3.709, and 1.186 mg/g), $1/n$ (1.3187, 0.9528, and 2.4946), and correlation coefficients were 0.9925, 0.9952, and 0.9376, respectively (Figure 14a–c).

As shown in Table 2, the Q_{max} derived from the Langmuir isotherm of alumina/NiO NCS was 16.58 mg/g and the pore volume was 0.86 $cm^3\ g^{-1}$. The capacity of adsorbents to absorb F^- ions varies, depending on their composition and textural properties. This capacity is linked to the pore diameter of the adsorbent. The alumina/NiO NCS had the highest F^- ion removal capacity, while the samples with smaller pore diameters had lower F^- ion removal capacities.[81]

Traditional adsorbents have progressively shown their particular application value and limitations during lengthy periods of usage and development. In contrast to the use of new adsorbents, research has mainly focused on synthesizing complexes of two or more adsorbents to create synergistic fluoride adsorption. Because different metal oxide adsorbents have different strengths and limitations for fluoride removal, current research investigations have used multimetal oxide. In comparison to ordinary metal oxides, multimetal oxides

https://doi.org/10.1021/acsomega.3c09076
ACS Omega 2024, 9, 23220−23240

frequently include several valence cations, offering additional chemisorption sites.[82] The tunability of each element's chemistry ensures an abundance of active sites, and the components can be adjusted to each other, possessing different outstanding properties and thus having unique quantum coupling effect and synergistic effects, resulting in high adsorption capacity.

3.5. Thermodynamic Studies. Temperature is an important factor in adsorption. In this scenario, the influence of temperature is investigated at five distinct temperatures: 298, 308, 318, and 328 K. Temperature affects the effect of alumina NPs, NiO NPs, and alumina/NiO NCS on the removal of fluoride ions in drinking water, which is explained by thermodynamic factors. The changes in Gibbs free energy (ΔG°, kJ/mol), enthalpy (ΔH°, kJ/mol), and entropy (ΔS°, kJ/mol) are evaluated to determine whether adsorption is spontaneous, endothermic, or exothermic.

The formulas of adsorption thermodynamics are 9−11[83]

$$\Delta G^\circ = -RT \ln(K_c) \tag{9}$$

$$\ln(K_c) = \frac{\Delta S^\circ}{R}\frac{\Delta H^\circ}{RT} \tag{10}$$

$$K_c = \frac{Q_e}{C_e} \tag{11}$$

R, T, and K_c are the molar gas constant (8.314 J K mol^{-1}), temperature (K), and thermodynamic constant, respectively.

Figure 15 illustrates the thermodynamic graphs for fluoride ion adsorption on the surface of alumina NPs, NiO NPs, and alumina/NiO NCS. The slope and intercept of the provided graphs were used to estimate the values of ΔH° and ΔS°, and the data are summarized in Table 3.

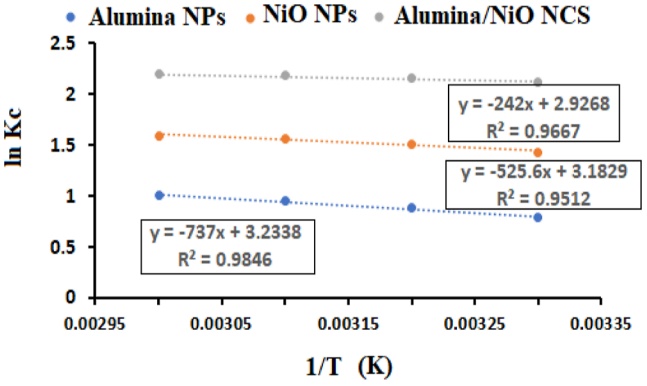

Figure 15. Thermodynamic plots of fluoride adsorption on the surfaces of alumina NPs, NiONPs, and alumina/NiO NCS.

The parameter ΔG° was used to study the physical adsorption or chemisorption in the process. Adsorption occurs spontaneously when ΔG° value is negative. Positive ΔH° values indicate that the process is endothermic. Positive ΔS° values indicate an increase in disorder at the solid−liquid interface during adsorption.[84] The nature of the adsorption process is described by the ΔH° value. ΔH° in the current study corresponded to 6.127, 4.369, and 2.011 J/mol for alumina NPs, NiO NPs, and alumina/NiO NCS, respectively, indicating a physicochemical adsorption process rather than a purely physical or chemical adsorption mechanism. The ΔS° values in this study were 26.885, 26.642, and 24.333 (J K^{-1} mol^{-1}). Endothermic and random adsorptions are indicated by positive ΔH° values. The maximum ΔG° values of −2.813, −4.342, and −5.989 J/mol indicate a physical adsorption process with electrostatic interaction between sorption sites and fluoride ions.

3.6. Probable Adsorption Mechanism. To verify the adsorption mechanism of F^- ions on the surface of presynthesized nanosorbents, a series of confirmatory analyses were performed using alumina/NiO NCS as an example. FT-IR analysis was performed before and after the adsorption of F ions on the surface of alumina/NiO NCS. A strong and broad peak at 3450 cm^{-1} was observed, which was attributed to the stretching vibration of the O−H absorption of Al $(OH)_3$. The peak of bent H−O−H was observed at 1641 cm^{-1}. A sharp peak was observed at 1020 cm^{-1} corresponding to the Al−O−H bonding. However, the sharp peak at 605 cm^{-1} was attributed to the formation of Al−F−Al[85] (Figure 16a). The XRD patterns of the sample before and after adsorption were essentially identical, indicating good stability, and the crystalline structure of the nanocomposite was not changed after the F^- ion adsorption process (Figure 16b,c). The SEM spectra of alumina/NiO NCS after adsorption did not change, indicating good stability of the crystalline structure of the nanosorbents (Figure 16d).

The XPS analysis was also performed after the process of adsorption of the F^- ions. Scanning XPS examination of the samples before and after the adsorption of fluoride and regeneration shows the presence of a fluoride peak at 690 eV after adsorption, while the peak disappeared after regeneration of the sample (Figure 17a). The binding energies of the two alumina/NiO NCS before and after the adsorption of fluoride were calculated. The results showed the atomic % of C 1s (30.67 and 23.98%), O 1s (42.04 and 36.24%), Al 2p (18.09 and

Table 3. Thermodynamic Parameters of Fluoride Adsorption of the Surface of Alumina NPs, NiO NPs, and Alumina/NiO NCS

adsorbents	C_0 (mg/L)	T (K)	ΔG° J/mol	ΔH° J/mol	ΔS° J K^{-1} mol^{-1}	R^2
alumina NPs	20	298	−1.960	6.127	26.885	0.9846
		308	−2.275			
		318	−2.534			
		328	−2.813			
NiO NPs	20	298	−3.560	4.369	26.462	0.9512
		308	−3.871			
		318	−4.149			
		328	−4.342			
alumina/NiO NCS	20	298	−5.289	2.011	24.333	0.96675
		308	−5.527			
		318	−5.767			
		328	−5.989			

https://doi.org/10.1021/acsomega.3c09076
ACS Omega 2024, 9, 23220−23240

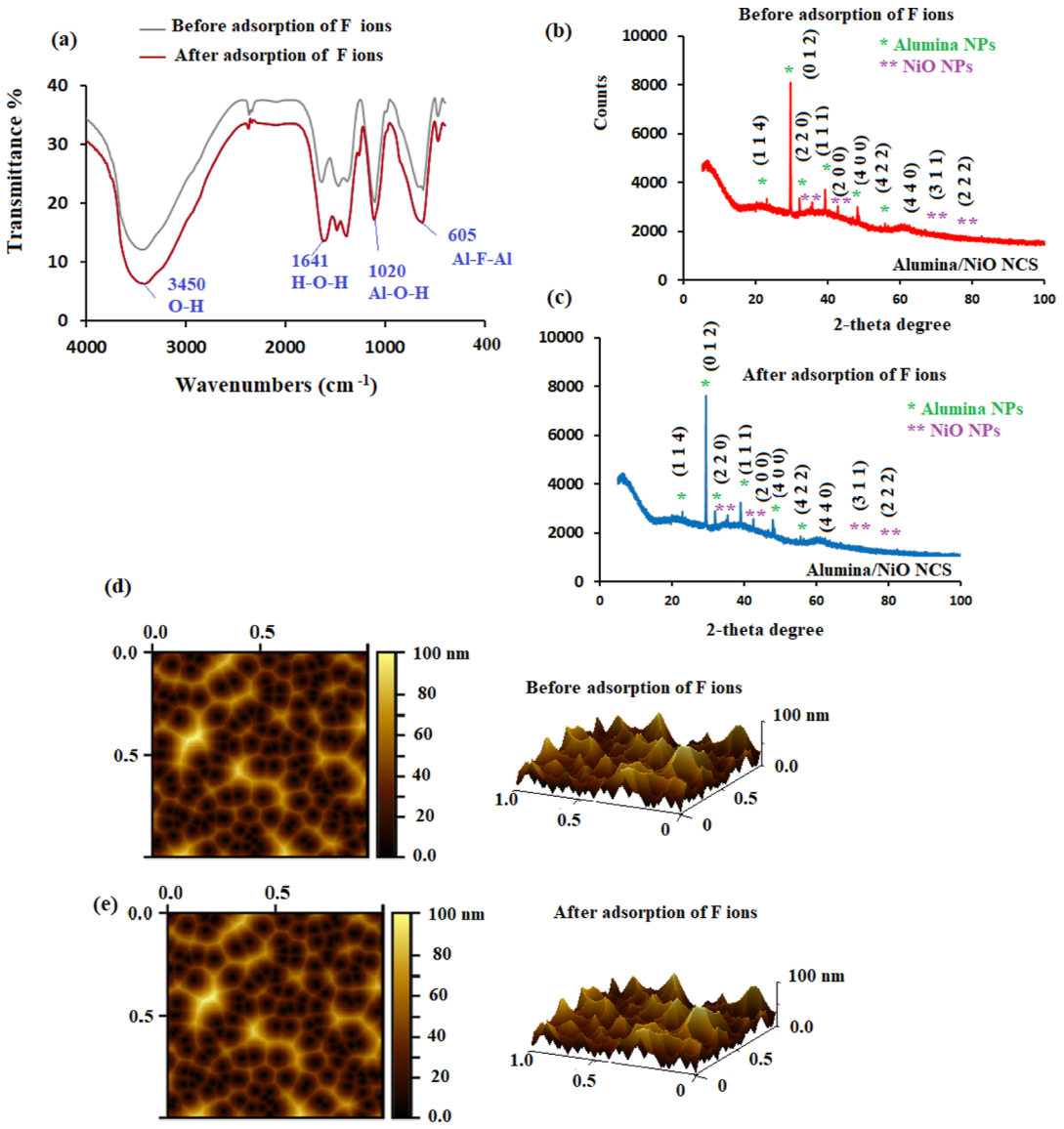

Figure 16. (a) FT-IR, (b,c) XRD patterns, and (d,e) SEM/AFM images before and after adsorption of F ions on the surface of alumina/NiO NCS.

17.20%), and Ni 2p (9.20 and 9.05%) after and before the adsorption process, respectively. In addition, the F ions were found to be 13.53% after adsorption. The fitted spectra show the presence of an oxide peak at binding energies of 75.19 and 76.22 eV, which could be attributed to aluminum oxide and aluminum hydroxide, respectively. Since aluminum fluoride has formed, the binding energy of 77.44 eV can be seen at this point (Figure 17b–d). The mechanism of adsorption by aluminum hydroxyl can be confirmed by this bond between aluminum fluoride. The highly electronegative electrostatic adsorption between the protonated functional groups and the fluoride favors this mechanism. In other words, according to Pearson's principle of hardness and softness of acid and base, hard acids preferentially coordinate with hard bases. Ni^{2+} was characterized as borderline, F^{-} was a hard acid, and Al^{3+} was a hard acid (Figure 17e–g).

3.7. Application of Contaminated Water Samples and Regeneration of Adsorbents. Six water samples with a fluoride concentration of 20 mg/L were analyzed. The results showed that alumina NPs, NiO NPs, and alumina/NiO NCS were effective in removing fluoride. In addition, the regeneration of the proposed adsorbents was also tested. The adsorbent used was filtered and sonicated with 5 mL of ethanol for 5 min and then 5 mL of deionized water was added, filtered, and dried in an oven at 100 °C for 1 h. The initial removal efficiency was assumed to be 100%, and the subsequent performance was approximated. The average efficiencies of alumina NPs, NiO NPs, and alumina/NiO NCS were 92.93, 95.59, and 98.61%, with RSD values of 0.17, 0.19, and 0.22%, respectively. However, the lowest efficiencies were 72.5, 86.7, and 89.4% for the above sorbent, respectively. These results indicate that the penetration of fluoride ions into the internal sorbent sites was easy and hindered the recovery (Figure 18).

A comparative study was conducted between the green synthesized nanosorbents and the previously developed alumina-based sorbents, and the comparative data are summarized in Table 4. The results of the present work under optimal experimental conditions (298 K temperature, 2 h contact time, and pH 7) confirmed that the proposed sorbents with a low dose of 0.8 g/L enable efficient removal of fluoride ions with removal efficiencies 92.93, 95.59, and 98.61% for the synthesized alumina NPs, NiO NPs, and alumina/NiO NCS,

https://doi.org/10.1021/acsomega.3c09076
ACS Omega 2024, 9, 23220−23240

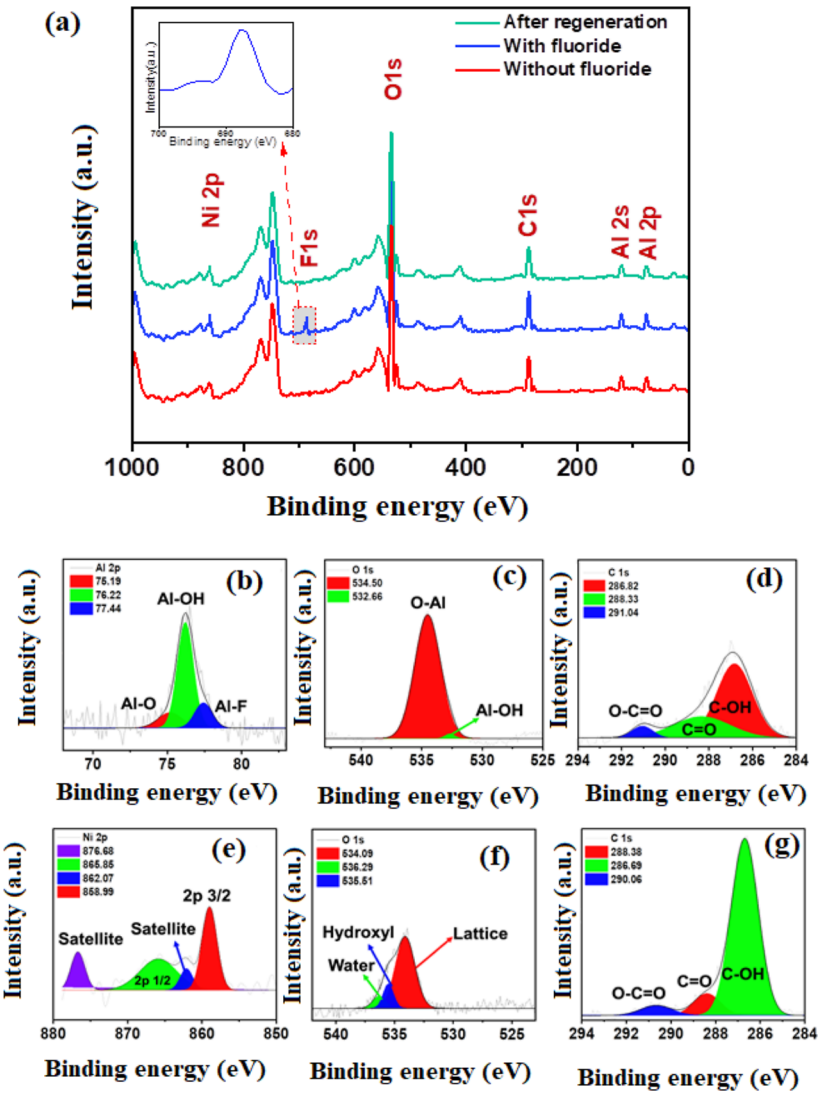

Figure 17. (a) XPS spectra survey, (b) Al 2p, (c) O 1s, (d) C 1s for alumina NPs, (e) Ni 2p, (f) O 1s, and (g) C 1s for NiO NPs before and after adsorption of F ions.

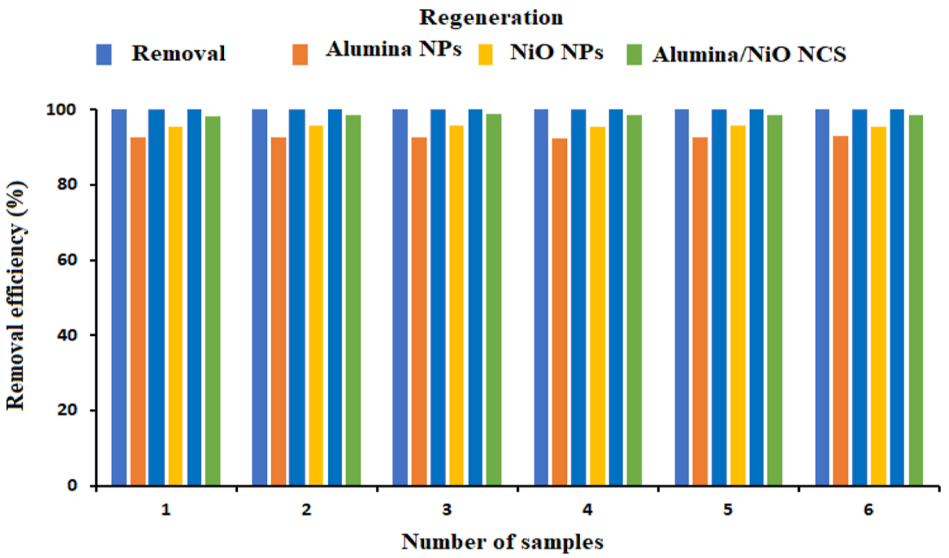

Figure 18. Removal % and regeneration % of six fluoride samples.

https://doi.org/10.1021/acsomega.3c09076
ACS Omega 2024, 9, 23220−23240

Table 4. Comparison between the Synthesized Nanomaterials and the Previously Reported Alumina-Based Sorbents for the Removal Efficiency of Fluoride Ions

	adsorption conditions								
adsorbents	initial C_{F^-} (mg/L)	pH	Temp. (K)	contact time (min)	sorbent dosage (g/L)	isotherm model	removal efficiency (%)	regeneration cycles	ref
β-CD@AlFuMoF	30	2	303	120	0.75	Langmuir	94.5%	7th	86
activated alumina	10	6−8	318	120	2.0	Freundlich	87.6%		87
nano γ alumina	8	4	303	120	1.0	Freundlich	96.0%	5th	88
Fe−Al bimetallic metal−organic-framework	10	7	303	45	1.0	Langmuir Freundlich	95.6%	8th	89
heterogeneous Al^{3+} modified mine-waste	10	7	303	60	10	Langmuir	84.0%		90
Cu^{2+} engrafted $MgAl_2O_4$	10	7	300	45	1.5	Langmuir	97.0%	3rd	91
aluminum fumarate MOF	30	7	293	60	0.75	Freundlich	100%		92
alumina NPs	20	7	298	120	0.8	Langmuir	92.93%	6th	current study
NiO NPs	20	7	298	120	0.8	Langmuir	95.59%	6th	
alumina/NiO NCS	20	7	298	120	0.8	Langmuir	98.61%	6th	

respectively. The experimental conditions of the present work are consistent with the other described methods[86−92] with respect to the Langmuir adsorption isotherm model. The advantage of the current method is that the removal efficiency can be carried out in a wide pH range of 2−8. Therefore, the synthesized alumina NPs, NiO NPs, and alumina/NiO NCS can be used as ideal adsorbents for the removal of fluoride from groundwater runoff even if the water is alkaline.

4. CONCLUSIONS

This study aimed to remove F^- ions from drinking water by using green nanosorbents (alumina NP, NiO NP, and alumina/NiO NCS). The adsorption process was found to be influenced by the initial pH of the solution, the dose of the adsorbent, and the concentration of fluoride ions, according to the results. Consequently, at neutral pH = 7, the removal effectiveness of alumina-NP, NiO-NP, and alumina/NiO NCS was the highest (67, 85, and 94%, respectively) when the adsorbent dose (0.8 g/L) and initial fluoride content (Co, 20 mg/L) increased. The adsorption isotherm of fluoride by alumina NP, NiO NP, and alumina/NiO NCS was effectively characterized by the Langmuir isotherm with Q_{max} values (12.53, 11.49, and 16.58 mg/g). Fluoride adsorption by alumina NP, NiO NP, and alumina/NiO-NCS was characterized using a pseudo-second-order kinetic model. The presence of positive ΔH° (6.127, 4.369, and 2.011 J/mol) for alumina NP, NiO NP, and alumina/NiO NCS, respectively, confirmed that the adsorption process was endothermic. In addition, positive ΔS° values (26.885, 26.462, and 24.333 kJ/mol) indicate an increase in disorder at the solid−liquid interface during adsorption. The formed nanomaterials can remove a considerable amount of fluoride in the pH range of 7, which makes them suitable for use in the defluoridation of drinking water. Plant-mediated adsorption synthesis can be presented as a cost-effective and environmentally acceptable adsorbent for environmental remediation and fluoride removal.

■ ASSOCIATED CONTENT

Data Availability Statement

All data have been included within the text.

■ AUTHOR INFORMATION

Corresponding Author

Seham S. Alterary − *Department of Chemistry, College of Science, King Saud University, Riyadh 11495, Saudi Arabia;* orcid.org/0000-0002-4176-2840; Email: salterary@ksu.edu.sa

Complete contact information is available at: https://pubs.acs.org/10.1021/acsomega.3c09076

Author Contributions

S.S.A. conceived and designed the experiments; analysis tools or data curation, wrote the paper; performed the experiments; and contributed reagents and materials. The author has read and agreed to the published version of the manuscript.

Notes

The author declares no competing financial interest.

■ ACKNOWLEDGMENTS

The authors provide great appreciation for Research Supporting Project, King Saud University, for supporting this study RSP2024R195.

■ REFERENCES

(1) Ali, H.; Khan, E.; Ilahi, I. Environmental chemistry and ecotoxicology of hazardous heavy metals: environmental persistence, toxicity, and bioaccumulation. *J. Chem.* **2019**, *2019*, 6730305.

(2) Verma, A.; Gupta, A.; Rajamani, P. Application of Wastewater in Agriculture: Benefits and Detriments. In *River Conservation and Water Resource Management*; Springer Nature Singapore: Singapore, 2023; pp 53−75.

(3) Berendes, D. M.; Fagerli, K.; Kim, S.; Nasrin, D.; Powell, H.; Kasumba, I. N.; Tennant, S. M.; Roose, A.; Jahangir Hossain, M.; Jones, J. C. M.; Zaman, S. M.; et al. Survey-based assessment of water, sanitation, and animal-associated risk factors for moderate-to-severe diarrhea in the Vaccine Impact on Diarrhea in Africa (VIDA) study: The Gambia, Mali, and Kenya, 2015−2018. *Clin. Infect. Dis.* **2023**, *76*, S132−S139.

(4) Wolf, J.; Johnston, R. B.; Ambelu, A.; Arnold, B. F.; Bain, R.; Brauer, M.; Brown, J.; Caruso, B. A.; Clasen, T.; Colford, J. M.; et al. Burden of disease attributable to unsafe drinking water, sanitation, and hygiene in domestic settings: a global analysis for selected adverse health outcomes. *Lancet* **2023**, *401*, 2060−2071.

(5) Rambabu, K.; Hai, A.; Bharath, G.; Thanigaivelan, A.; Kui, C. C.; Hasan, S. W.; Banat, F. Biocompatible nanomater ials for sensing and

remediation of nitrites and fluorides from polluted water. In *Advances in Nano and Biochemistry*; Academic Press, 2023; pp 57−84.
(6) Ahmad Dar, F.; Kurella, S. Fluoride in drinking water: An in-depth analysis of its prevalence, health effects, advances in detection and treatment. *Mater. Today: Proc.* **2023**.
(7) Abolli, S.; Yaghmaeian, K.; Arab Aradani, A.; Alimohammadi, M. Comparing groundwater fluoride level with WHO guidelines and classifying at-risk age groups; based on health risk assessment. *Int. J. Environ. Anal. Chem.* **2023**, *103*, 747−760.
(8) Bibi, S.; Habib, R.; Shafiq, S.; Abbas, S. S.; Khan, S.; Eqani, S. A. M. A. S.; Nepovimova, E.; Khan, M. S.; Kuca, K.; Nurulain, S. M. Influence of the chronic groundwater fluoride consumption on cholinergic enzymes, ACHE and BCHE gene SNPs and pro-inflammatory cytokines: A study with Pakistani population groups. *Sci. Total Environ.* **2023**, *880*, 163359.
(9) Mhamdi, M.; Mahjoubi, N.; Azizi, M.; Elaloui, E.; Trabelsi-Ayadi, M. Towards an Efficient Purification Process of Nanostructured Materials: Investigation of Raw Tunisian Clay for Defluoridation of Natural Water. *Water Air Soil Poll.* **2023**, *234*, 234.
(10) Hu, J.; Song, J.; Han, X.; Wen, Q.; Yang, W.; Pan, W.; Jian, S.; Jiang, S. Fabrication of Ce-La-MOFs for defluoridation in aquatic systems: A kinetics, thermodynamics and mechanisms study. *Sep. Purif. Technol.* **2023**, *314*, 123562.
(11) Singh, N.; Dhillon, A.; Kumar, D. Metal-organic frameworks for adsorption of fluoride for groundwater treatment. *Groundw. Sustain. Dev.* **2023**, *23*, 100967.
(12) Saharan, P.; Kumar, V.; Kaushal, I.; Mittal, A.; Shukla, S. K.; Kumar, D.; Sharma, A. K.; Om, H. A comprehensive review on the metal-based green valorized nanocomposite for the remediation of emerging colored organic waste. *Environ. Sci. Poll. Res.* **2023**, *30*, 45677−45700.
(13) Nivedhitha, D. M.; Jeyanthi, S. Polyvinylidene fluoride—An advanced smart polymer for electromagnetic interference shielding applications—A novel review. *Polym. Adv. Technol.* **2023**, *34*, 1781−1806.
(14) Chaudhary, M.; Rawat, S.; Maiti, A. Defluoridation by bare nanoadsorbents, nanocomposites, and nanoadsorbent loaded mixed matrix membranes. *Sep. Purif. Rev.* **2023**, *52*, 135−153.
(15) Liu, W.; Liao, N.; Nath, M.; Li, Y.; Dai, Y.; Pan, L. Effects of characteristic hydrates on the pore structure and fracture behavior of CAC bonded alumina-spinel castables. *Const. Build. Mater.* **2023**, *389*, 131736.
(16) Hussain, S.; Ali Muazzam, M.; Ahmed, M.; Ahmad, M.; Mustafa, Z.; Murtaza, S.; Ali, J.; Ibrar, M.; Shahid, M.; Imran, M. Green synthesis of nickel oxide nanoparticles using Acacia nilotica leaf extracts and investigation of their electrochemical and biological properties. *J. Taibah Univ. Sci.* **2023**, *17*, 2170162.
(17) Coloma, A.; Velty, A.; Díaz, U. Hybrid organic−inorganic nanoparticles with associated functionality for catalytic transformation of biomass substrates. *RSC Adv.* **2023**, *13*, 10144−10156.
(18) Hirschbiegel, C. M.; Zhang, X.; Huang, R.; Cicek, Y. A.; Fedeli, S.; Rotello, V. M. Inorganic nanoparticles as scaffolds for bioorthogonal catalysts. *Adv. Drug Delivery Rev.* **2023**, *195*, 114730.
(19) Cai, X.; Wang, Z.; Xing, Y.; Zheng, C.; Yan, P.; Bao, W.; Xie, T.; Hu, Y.; Deng, Y.; Zhang, Y.; Wu, Y.; et al. Promotion of the Nucleation of Ultrafine Ni-Rich Layered Oxide Primary Particles by an Atomic Layer-Deposited Thin Film for Enhanced Mechanical Stability. *Nano Lett.* **2023**, *23*, 5770−5778.
(20) Su, Z.; Yi, S.; Zhang, W.; Xu, X.; Zhang, Y.; Zhou, S.; Niu, B.; Long, D. Ultrafine vacancy-rich Nb_2O_5 semiconductors confined in carbon nanosheets boost dielectric polarization for high-attenuation microwave absorption. *Nano-Micro Lett.* **2023**, *15*, 183.
(21) Hwang, Y. G.; Nulu, V.; Nulu, A.; Sohn, K. Y. Hollow nanostructured NiO particles as an efficient electrode material for lithium-ion energy storage properties. *RSC Adv.* **2023**, *13*, 22007−22016.
(22) Hamdan, A. M.; Sardi, A.; Reksamunandar, R. P.; Maulida, Z.; Arsa, D. A.; Lubis, S. S.; Nisah, K. Green synthesis of NiO nanoparticles using a Cd hyperaccumulator (Lactuca sativa L.) and its application as a Pb (II) and Cu (II) adsorbent. *Environ. Nanotechnol. Monit. Manag.* **2024**, *21*, 100910.
(23) Ferenj, A. E.; Kabtamu, D. M.; Assen, A. H.; Gedda, G.; Muhabie, A. A.; Berrada, M.; Girma, W. M. Hagenia abyssinica-Biomediated Synthesis of a Magnetic Fe_3O_4/NiO Nanoadsorbent for Adsorption of Lead from Wastewater. *ACS Omega* **2024**, *9*, 6803−6814.
(24) Zhou, X.; Jia, Z.; Zhang, X.; Wang, B.; Wu, W.; Liu, X.; Xu, B.; Wu, G. Controllable synthesis of Ni/NiO@ porous carbon hybrid composites towards remarkable electromagnetic wave absorption and wide absorption bandwidth. *J. Mater. Sci. Technol.* **2021**, *87*, 120−132.
(25) Al-Hazmi, G. H.; Refat, M. S.; El-Desouky, M. G.; Wali, F. K.; El-Bindary, A. A. Effective removal of industrial dye from aqueous solution using mesoporous nickel oxide: a complete batch system evaluation. *Desalin. Water Treat.* **2022**, *273*, 246−260.
(26) Rajendran, S.; Priya, A. K.; Senthil Kumar, P.; Hoang, T. K.; Sekar, K.; Chong, K. Y.; Khoo, K. S.; Ng, H. S.; Show, P. L. A critical and recent developments on adsorption technique for removal of heavy metals from wastewater-A review. *Chemosphere* **2022**, *303*, 135146.
(27) Mudassir, M. A.; Hussain, S. Z.; Kousar, S.; Zhang, H.; Ansari, T. M.; Hussain, I. Hyperbranched polyethylenimine-tethered multiple emulsion-templated hierarchically macroporous poly (acrylic acid)−Al_2O_3 nanocomposite beads for water purification. *ACS Appl. Mater. Interfaces* **2021**, *13*, 27400−27410.
(28) Alburaih, H. A.; Aadil, M.; Mubeen, S.; Hassan, W.; Rabia Ejaz, S.; Anwar, A.; Aman, S.; Alsafari, I. A. Facile synthesis of $W_{1-y}FeyO_3$@ NiO@ RGO ternary nanohybrid with enhanced sunlight mediated photocatalytic and bactericidal activities for water purification. *FlatChem* **2022**, *34*, 100380.
(29) Nair, G. M.; Sajini, T.; Mathew, B. Advanced green approaches for metal and metal oxide nanoparticles synthesis and their environmental applications. *Talanta Open* **2022**, *5*, 100080.
(30) Md Ishak, N. A. I.; Kamarudin, S. K.; Timmiati, S. N. Green synthesis of metal and metal oxide nanoparticles via plant extracts: an overview. *Mater. Res. Exp.* **2019**, *6*, 112004.
(31) Mondal, P.; Purkait, M. K. Preparation and characterization of novel green synthesized iron−aluminum nanocomposite and studying its efficiency in fluoride removal. *Chemosphere* **2019**, *235*, 391−402.
(32) Biftu, W. K.; Mekala, S.; Ravindhranath, K. De-fluoridation of Polluted Water Using Aluminium Alginate Beads Doped with Green Synthesized 'Nano SiO_2' Nano CeO_2-ZrO_2', as an Effective Adsorbent. *ChemistrySelect* **2020**, *5*, 15061−15074.
(33) Singh, N.; Kumari, S.; Goyal, N.; Khan, S. Al_2O_3/GO cellulose based 3D-hydrogel for efficient fluoride removal from water. *Environ. Nanotechnol. Monit. Manag.* **2021**, *15*, 100444.
(34) Yang, W.; Tian, S.; Tang, Q.; Chai, L.; Wang, H. Fungus hyphae-supported alumina: an efficient and reclaimable adsorbent for fluoride removal from water. *J. Colloid Interface Sci.* **2017**, *496*, 496−504.
(35) Afonso, A. F.; Pereira, O. R.; Fernandes, A.; Calhelha, R. C.; Silva, A. M.; Ferreira, I. C.; Cardoso, S. M. Phytochemical composition and bioactive effects of Salvia africana, Salvia officinalis 'Icterina'and Salvia mexicana aqueous extracts. *Molecules* **2019**, *24*, 4327.
(36) Alhamad, A. A.; Zeghoud, S.; Amor, I. B.; Zaater, A.; Amor, A. B.; Aouadif, A.; Hemmami, A. AA short review of nanomaterials: synthesis methods, properties, and applications. *Algerian J. Chem. Eng.* **2023**, *1*, 01−07.
(37) Sabouri, Z.; Akbari, A.; Hosseini, H. A.; Khatami, M.; Darroudi, M. Green-based biosynthesis of nickel oxide nanoparticles in Arabic gum and examination of their cytotoxicity, photocatalytic and antibacterial effects. *Green Chem. Lett. Rev.* **2021**, *14*, 404−414.
(38) Gholizadeh, Z.; Aliannezhadi, M.; Ghominejad, M.; Tehrani, F. S. High specific surface area γ-Al2O3 nanoparticles synthesized by facile and low-cost co-precipitation method. *Sci. Rep.* **2023**, *13*, 6131.
(39) Bhosale, S. R.; Shinde, S. B.; Bhosale, R. R.; Dhengale, S. D.; Moyo, A. A.; Dhavale, R. P.; Anbhule, P. V. Antibacterial Efficacy of NiO Composites with CuO Nanoclusters via Coprecipitation Method. *Inorg. Chem. Commun.* **2023**, *155*, 111059.
(40) Martins, N.; Barros, L.; Santos-Buelga, C.; Henriques, M.; Silva, S.; Ferreira, I. C. Evaluation of bioactive properties and phenolic

https://doi.org/10.1021/acsomega.3c09076
ACS Omega 2024, 9, 23220−23240

compounds in different extracts prepared from *Salvia officinalis* L. *Food Chem.* **2015**, *170*, 378−385.
(41) Al-Humud, N. S.; Al-Tamimi, S. A.; Al-Mohaimeed, A. M.; El-Tohamy, M. F. Comparative Study for Spectrofluorimetric Determination of Ambroxol Hydrochloride Using Aluminum Metal Transfer Chelation Complex and Biogenic Synthesis of Aluminum Oxide Nanoparticles Using Lavandula spica Flowers Extract. *Molecules* **2023**, *28*, 2210.
(42) Alshehri, E. M.; Alarfaj, N. A.; Al-Tamimi, S. A.; El-Tohamy, M. F. Electroanalytical sensors-based biogenic synthesized metal oxide nanoparticles for potentiometric assay of pantoprazole sodium. *Green Chem. Lett. Rev.* **2023**, *16*, 2240837.
(43) El-Feky, A. M.; Aboulthana, W. M. Phytochemical and biochemical studies of sage (Salvia officinalis L.). *Pharm. Biosci. J.* **2016**, *4*, 56−62.
(44) Modaresahmadi, K.; Khodadoust, A. P.; Wescott, J. Adsorption of fluoride from water using Al−Mg−Ca ternary metal oxide-coated sand. *Water Supply* **2023**, *23*, 4699−4713.
(45) Fannang, S. V.; Tankeu, S. E.; Etame Loe, G. M. M.; Yinyang, J.; Ngouondjou Foze, T.; Bamal, H. D.; Mbida Mvomo, B. D. Phytochemical screening and study of the acute oral toxicity of the aqueous extract of the leaves of Diospyros hoyleana F.white (Ebenaceae). *Saudi J. Med. Pharm. Sci.* **2021**, *7*, 230−235.
(46) Benzeggouta, N. Evaluation des effets biologiques des extraits aqueux de plantes medicinales seules et combinées. Ph.D. Dissertation, Mentouri-Constantine University: Constantine, Algeria, 2017.
(47) Adusei, S.; Otchere, J. K.; Oteng, P.; Mensah, R. Q.; Tei-Mensah, E. Phytochemical analysis, antioxidant and metal chelating capacity of *Tetrapleura tetraptera*. *Heliyon* **2019**, *5*, No. e02762.
(48) Jaradat, N.; Hussen, F.; Al Ali, A. Preliminary phytochemical screening, quantitative estimation of total flavonoids, total phenols and antioxidant activity of *Ephedra alata* decne. *J. Mater. Environ. Sci.* **2015**, *6*, 1771−1778.
(49) Sahu, A.; Sen, S.; Mishra, S. C. Processing and properties of Calotropis gigantea bio-char: A wasteland weed. *Mater. Today: Proc.* **2020**, *33*, 5334−5340.
(50) Khoshraftar, Z.; Safekordi, A. A.; Shamel, A.; Zaefizadeh, M. Synthesis of natural nanopesticides with the origin of *Eucalyptus globulus* extract for pest control. *Green Chem. Lett. Rev.* **2019**, *12*, 286−298.
(51) Oueslati, M. H.; Ben Tahar, L.; Harrath, A. H. Synthesis of ultra-small gold nanoparticles by polyphenol extracted from *Salvia officinalis* and efficiency for catalytic reduction of p-nitrophenol and methylene blue. *Green Chem. Lett. Rev.* **2020**, *13*, 18−26.
(52) Einafshar, N.; Amiri Farmad, H.; Moshirian Farahi, S. M.; Einafshar, E. Nanocomposite with high adsorption activity developed using stabilized silver modified alumina and TiO_2-NPs incorporated into β-cyclodextrin-graphene oxide. *Heliyon* **2023**, *9*, No. e18162.
(53) Balciunaitienė, A.; Liaudanskas, M.; Puzeryte, V.; Viskelis, J.; Janulis, V.; Viskelis, P.; Griskonis, E.; Jankauskaite, V. Eucalyptus globulus and Salvia officinalis extracts mediated green synthesis of silver nanoparticles and their application as an antioxidant and antimicrobial agent. *Plants* **2022**, *11*, 1085.
(54) Hodoroaba, V. D. Energy-dispersive X-ray spectroscopy (EDS). In *Characterization of Nanoparticles*; Elsevier, 2020; pp 397−417.
(55) Sadeghi, A.; Toiserkani, H. Preparation and investigation of properties of deproteinized natural rubber nanocomposites incorporating functionalized nano-alumina by in situ emulsion polymerization. *J. Vinyl Add. Technol.* **2023**, *29*, 534−544.
(56) Akhavan-Bahabadi, Z.; Zare, H. R.; Mohammadpour, Z.; Mirjalili, B. B. F. Improvement of Anti-Corrosion Performance of a Cu-Ni Bimetallic Organic Framework Smart Coating Using Amino-Substitution Triazole. *ChemistrySelect* **2023**, *8*, No. e202300363.
(57) Garg, A.; Parmar, L. K.; Garg, T.; Dager, H. S.; Bhardwaj, P.; Yadav, A. Structural analysis and dielectric behavior of low-temperature synthesized nickel cobaltite. *Chem. Phys. Impact* **2024**, *8*, 100457.
(58) Yang, Q.; Cao, J.; Ding, R.; Zhan, K.; Yang, Z.; Zhao, B.; Wang, Z.; Ji, V. The synthesis and mechanism of superhydrophobic coatings with multifunctional properties on aluminum alloys surface: a review. *Prog. Org. Coat.* **2023**, *184*, 107875.
(59) Fu, Q.; Yan, L.; Liu, D.; Zhang, S.; Jiang, H.; Xie, W.; Yang, L.; Wang, Y.; Wang, H.; Zhao, X. Highly-dispersed surface NiO species and exposed Ni (200) facets facilitating activation of furan ring for high-efficiency total hydrogenation of furfural. *Appl. Catal., B* **2024**, *343*, 123501.
(60) AL-Salman, H. N. K.; Falih, M. s.; Deab, H. B.; Altimari, U. S.; Shakier, H. G.; Dawood, A. H.; Ramadan, M. F.; Mahmoud, Z. H.; Farhan, M. A.; Koten, H.; Kianfar, E. A study in analytical chemistry of adsorption of heavy metal ions using chitosan/graphene nano-composites. *Chem. Environ. Eng.* **2023**, *8*, 100426.
(61) Nikolic, G. S.; Simonovic, N.; Nikolic, L.; Durmisevic, M.; Marković-Nikolić, D.; Ristic, N.; Bojic, A. An integrated OVAT-RSM design to gaps-filling in the study of phosphate sorption process onto cationic modified bottle gourd shell. *Adv. Technol.* **2023**, *12*, 5−19.
(62) Zeng, Z.; Li, Q.; Yan, J.; Huang, L.; Arulmani, S. R. B.; Zhang, H.; Xie, S.; Sio, W. The model and mechanism of adsorptive technologies for wastewater containing fluoride: A review. *Chemosphere* **2023**, *340*, 139808.
(63) Owusu-Agyeman, I.; Jeihanipour, A.; Luxbacher, T.; Schäfer, A. I. Implications of humic acid, inorganic carbon and speciation on fluoride retention mechanisms in nanofiltration and reverse osmosis. *J. Membr. Sci.* **2017**, *528*, 82−94.
(64) George, S.; Pandit, P.; Gupta, A. B. Residual aluminium in water defluoridated using activated alumina adsorption−Modeling and simulation studies. *Water Res.* **2010**, *44*, 3055−3064.
(65) Theiss, F. L.; Couperthwaite, S. J.; Ayoko, G. A.; Frost, R. L. A review of the removal of anions and oxyanions of the halogen elements from aqueous solution by layered double hydroxides. *J. Colloid Interface Sci.* **2014**, *417*, 356−368.
(66) Kumar, K. V.; Gadipelli, S.; Howard, C. A.; Kwapinski, W.; Brett, D. J. Probing adsorbent heterogeneity using Toth isotherms. *J. Mater. Chem. A* **2021**, *9*, 944−962.
(67) Wu, Y.; Fang, S.; Zhang, J.; Mo, X.; Liu, L. A Review on Adsorption Mechanisms and Distribution Coefficient (Kd) of Cesium in Clay/Host Rock. *PBNC 2022, Beijing & Chengdu, China*; Springer, 2023; Vol. *2*, pp 898−912.
(68) Tangsir, S.; Hafshejani, L. D.; Lahde, A.; Maljanen, M.; Hooshmand, A.; Naseri, A. A.; Moazed, H.; Jokiniemi, J.; Bhatnagar, A. 2016. Water defluoridation using Al_2O_3 nanoparticles synthesized by flame spray pyrolysis (FSP) method. *Chem. Eng. J.* **2016**, *288*, 198−206.
(69) Kushwaha, A.; Arif, Z.; Singh, B. Adsorptive Removal of Fluoride from Water Using Iron Oxide-Hydrogen Nanoparticles. In *Advanced Treatment Technologies for Fluoride Removal in Water: Water Purification*; Springer Nature Switzerland: Cham, 2024; pp 139−157.
(70) Li, W.; Zu, B.; Li, J.; Li, L.; Li, J.; Mei, X. Microplaastics as potential bisphenol carriers: role of adsorbents, adsorbates, and environmental factors. *Environ. Sci. Poll. Res.* **2023**, *30*, 77139−77149.
(71) Elhalil, A.; Qourzal, S.; Mahjoubi, F. Z.; Elmoubarki, R.; Farnane, M.; Tounsadi, H.; Sadiq, M.; Abdennouri, M.; Barka, N. Defluoridation of groundwater by calcined Mg/Al layered double hydroxide. *Emerging Contam.* **2016**, *2*, 42−48.
(72) Kumar, E.; Bhatnagar, A.; Ji, M.; Jung, W.; Lee, S. H.; Kim, S. J.; Lee, G.; Song, H.; Choi, J. Y.; Yang, J. S.; Jeon, B. H. Defluoridation from aqueous solutions by granular ferric hydroxide (GFH). *Water Res.* **2009**, *43*, 490−498.
(73) Zavarize, D. G.; Vieira, G. E. G.; de Oliveira, J. D. Kinetics of free fatty acids esterification in waste frying oil using novel carbon-based acid heterogeneous catalyst derived from Amazonian Açaí seeds−Role of experimental conditions on a simpler pseudo first-order reaction mechanism. *Catal. Commun.* **2023**, *180*, 106716.
(74) Tran, H. N. Applying linear forms of pseudo-second-order kinetic model for feasibly identifying errors in the initial periods of time-dependent adsorption datasets. *Water* **2023**, *15*, 1231.
(75) Basharat, S.; Rehman, R.; Mitu, L. Adsorptive separation of brilliant green dye from water by tartaric acid-treated *holarrhena antidysenterica* and *Citrullus colocynthis* biowaste. *J. Chem.* **2021**, *2021*, 1−18.

https://doi.org/10.1021/acsomega.3c09076
ACS Omega 2024, 9, 23220−23240

(76) Hassaan, M. A.; Yılmaz, M.; Helal, M.; El-Nemr, M. A.; Ragab, S.; El Nemr, A. Improved methylene blue adsorption from an aqueous medium by ozone-triethylenetetramine modification of sawdust-based biochar. *Sci. Rep.* **2023**, *13*, 12431.
(77) Al nami, S. Y.; Hossan, A. Adsorption of triclosan from aqueous solutions via novel metal−organic framework: Adsorption isotherms, kinetics, and optimization via Box-Behnken design. *J. Mol. Liq.* **2023**, *382*, 122065.
(78) Amrutha, G. J.; Girish, C. R.; Prabhu, B.; Mayer, K. Multi-component Adsorption Isotherms: Review and Modeling Studies. *Environ. Proc.* **2023**, *10*, 38.
(79) Fouad, M. R. Effect of Temperature and Soil Type on the Adsorption and Desorption Isotherms of Thiamethoxam Using Freundlich Equation. *Egypt. J. Chem.* **2023**, *66*, 197−207.
(80) Hu, Q.; Lan, R.; He, L.; Liu, H.; Pei, X. A critical review of adsorption isotherm models for aqueous contaminants: Curve characteristics, site energy distribution and common controversies. *J. Environ. Manag.* **2023**, *329*, 117104.
(81) Ono, R.; Shimoda, S.; Fukuoka, A.; Takada, T. Fluoride removal from water using Zr-modified meso-and macroporous carbons: effect of pore structure and adsorption conditions. *Chem. Eng. J. Adv.* **2023**, *15*, 100512.
(82) Raghav, S.; Kumar, D. Adsorption Equilibrium, Kinetics, and Thermodynamic Studies of Fluoride Adsorbed by Tetrametallic Oxide Adsorbent. *J. Chem. Eng. Data* **2018**, *63*, 1682−1697.
(83) Du, Y.; Guo, T.; Geng, Y.; Zhang, R.; Kong, L.; Fan, Z.; Xiao, H. Adsorption thermodynamics of CO₂ on nitrogen-doped biochar synthesized with moderate temperature ionic liquid. *Can. J. Chem. Eng.* **2023**, *101*, 1772−1791.
(84) Abbou, B.; Lebkiri, İ.; Ouaddari, H.; Elkhattabi, O.; Habsaoui, A.; Lebkiri, A.; Rifi, E. H. Kinetic and thermodynamic study on adsorption of cadmium from aqueous solutions using natural clay. *J. Turk. Chem. Soc., Sect. A* **2021**, *8*, 677−692.
(85) Drouiche, N.; Ghaffour, N.; Aoudj, S.; Hecini, M.; Ouslimane, T. Fluoride removal from photovoltaic wastewater by aluminium electrocoagulation and characteristics of products. *Chem. Eng. Trans.* **2009**, *17*, 1651−1656.
(86) Ren, Y.; Wu, F.; Qu, G.; Ren, N.; Ning, P.; Chen, X.; He, M.; Yang, Y.; Wang, Z.; Hu, Y. Extraction and preparation of metal organic frameworks from secondary aluminum ash for removal mechanism study of fluoride in wastewater. *J. Mater. Res. Technol.* **2023**, *23*, 3023−3034.
(87) Dhawane, S. H.; Khan, A. A.; Singh, K.; Tripathi, A.; Hasda, R.; Halder, G. Insight into Optimization, isotherm, kinetics, and thermodynamics of fluoride adsorption onto activated alumina. *Environ. Prog. Sustain. Energy* **2018**, *37*, 766−776.
(88) Chinnakoti, P.; Chunduri, A. L.; Vankayala, R. K.; Patnaik, S.; Kamisetti, V. Enhanced fluoride adsorption by nano crystalline γ-alumina: adsorption kinetics, isotherm modeling and thermodynamic studies. *Appl. Water Sci.* **2017**, *7*, 2413−2423.
(89) Mukherjee, A.; Dhak, P.; Dhak, D. The solvothermal synthesis of a 3D rod-like Fe−Al bimetallic metal−organic-framework for efficient fluoride adsorption and photodegradation of water-soluble carcinogenic dyes. *Environ. Sci.: Adv.* **2022**, *1* (2), 121−137.
(90) Mukherjee, A.; Chowdhury, A.; Adak, M. K.; Khatun, J.; Dhak, P.; Dhak, D. Fluoride adsorption and photoreduction of Cr (VI) using heterogeneous Al3+ modified mine-waste, an in-situ approach. *J. Environ. Chem. Eng.* **2020**, *8* (3), 103759.
(91) Mukherjee, A.; Adak, M. K.; Dhak, P.; Dhak, D. A simple chemical method for the synthesis of Cu2+ engrafted $MgAl_2O_4$ nanoparticles: Efficient fluoride adsorbents, photocatalyst and latent fingerprint detection. *J. Environ. Sci.* **2020**, *88*, 301−315.
(92) Tolkou, A. K.; Zouboulis, A. I. Fluoride removal from water sources by adsorption on MOFs. *Separations* **2023**, *10*, 467.

https://doi.org/10.1021/acsomega.3c09076
ACS Omega 2024, 9, 23220−23240